

The Influence of Crustal Magnetic Fields on the Martian Bow Shock Location: A Statistical Analysis of MAVEN and Mars Express Observations

P. Garnier, C. Jacquey, X. Gendre, V. Génot, C. Mazelle, X. Fang, J. R. Gruesbeck, B. Sánchez-Cano, J. S. Halekas

▶ **To cite this version:**

P. Garnier, C. Jacquey, X. Gendre, V. Génot, C. Mazelle, et al.. The Influence of Crustal Magnetic Fields on the Martian Bow Shock Location: A Statistical Analysis of MAVEN and Mars Express Observations. Journal of Geophysical Research Space Physics, 2022, 127, 10.1029/2021JA030146 . insu-03867497

HAL Id: insu-03867497

https://insu.hal.science/insu-03867497

Submitted on 23 Nov 2022

HAL is a multi-disciplinary open access archive for the deposit and dissemination of scientific research documents, whether they are published or not. The documents may come from teaching and research institutions in France or abroad, or from public or private research centers.

L'archive ouverte pluridisciplinaire **HAL**, est destinée au dépôt et à la diffusion de documents scientifiques de niveau recherche, publiés ou non, émanant des établissements d'enseignement et de recherche français ou étrangers, des laboratoires publics ou privés.



Distributed under a Creative Commons Attribution 4.0 International License

Check for updates

JGR Space Physics

RESEARCH ARTICLE
10.1029/2021JA030146

Key Points:

- The influence of crustal magnetic fields on the Martian shock is significant based on the first multi-mission study
- The strongest crustal field region has a major influence in a large angular range, when close to noon and when the interplanetary magnetic field is stable
- The crustal field influence varies with season, showing a coupling between crustal fields, the ionosphere and the shock

Correspondence to:
P. Garnier,
philippe.garnier@irap.omp.eu

Citation:
Garnier, P., Jacquey, C., Gendre, X., Génot, V., Mazelle, C., Fang, X., et al. (2022). The influence of crustal magnetic fields on the Martian bow shock location: A statistical analysis of MAVEN and Mars Express observations. *Journal of Geophysical Research: Space Physics*, *127*, e2021JA030146. https://doi.org/10.1029/2021JA030146

Received 22 NOV 2021
Accepted 4 APR 2022

The copyright line for this article was changed on 14 JUN 2022 after original online publication.

© 2022. The Authors.
This is an open access article under the terms of the Creative Commons Attribution License, which permits use, distribution and reproduction in any medium, provided the original work is properly cited.

The Influence of Crustal Magnetic Fields on the Martian Bow Shock Location: A Statistical Analysis of MAVEN and Mars Express Observations

P. Garnier[1], C. Jacquey[1], X. Gendre[2], V. Génot[1], C. Mazelle[1], X. Fang[3], J. R. Gruesbeck[4,5], B. Sánchez-Cano[6], and J. S. Halekas[7]

[1]IRAP, Universite de Toulouse, CNES, CNRS, UPS, (Toulouse), Toulouse, France, [2]ISAE-SUPAERO, Universite de Toulouse, Toulouse, France, [3]Laboratory for Atmospheric and Space Physics, University of Colorado, Boulder, CO, USA, [4]Department of Astronomy, University of Maryland, College Park, MD, USA, [5]NASA Goddard Space Flight Center, Greenbelt, MD, USA, [6]School of Physics and Astronomy, University of Leicester, Leicester, UK, [7]Department of Physics and Astronomy, University of Iowa, Iowa City, IA, USA

Abstract Previous missions underlined the complex influence of the crustal magnetic fields on the Martian environment, including the plasma boundaries. Their influence on the bow shock is however poorly constrained, with most studies showing North/South differences attributed to the crustal fields, with various conclusions from little to strong variabilities. We analyze for the first time in detail the influence of crustal fields on the Martian shock location based on a multi-mission analysis (MAVEN and MEX). We introduce the angular distance to the strongest crustal field region in the southern hemisphere that induces the largest influence (but not unique, with a minimum pressure threshold analyzed). Its impact is at large scale (>40–60° around), is modulated by the local time of the strongest source region (with no influence beyond terminator), and maximizes when the Interplanetary Magnetic field (IMF) is stable during the preceding hours. We introduce a technique, that is, partial correlations, to provide a coherent picture for both MAVEN/MEX due to existing cross correlations with Extreme UltraViolet (EUV). A composite parameter is proposed, that represents the combined influence of EUV, magnetosonic mach number (two major drivers) and crustal fields, the latter having an impact of hundreds of km. The influence of crustal fields on the shock appears seasonal and correlated with the Total Electronic Content, revealing a large scale coupling between the crustal fields, the ionosphere and the shock. The crustal field influence on the shock is thus significant and complex, with a coupling to both the ionosphere below and the IMF above.

Plain Language Summary The Mars Express (MEX) and Mars Atmosphere and Volatile Evolution (MAVEN) observations underlined the complex interaction between the solar wind plasma flowing out from the Sun and the martian environment. The supersonic flow creates a bow shock upstream of the planet, before it is deflected around the conductive ionized atmosphere of the planet that acts as an obstacle to the flow. Contrary to Earth, Mars lost its intrinsic global dynamo magnetic field that could protect efficiently the atmosphere from the incident solar wind sputtering, thus eroding the atmosphere with time. However, the planet possesses remnant crustal magnetic fields locked up in its crust, in particular in the southern hemisphere, that are known to play a major role in the martian interaction with the incident solar wind. We investigate here the influence of these crustal fields on the martian bow shock location, and show they are a significant driver according to MAVEN and MEX observations, despite being less important than the solar Extreme UltraViolet fluxes or magnetosonic mach number of the solar wind. We also show that that this influence varies with season, revealing a strong coupling between the crustal fields, the ionosphere and the bow shock location.

1. Introduction

The Martian interaction with the solar wind (SW) is unique due to the absence of a global intrinsic dynamo magnetic field but with the presence of remnant crustal magnetic fields (Acuña et al., 2001). The Mars Global Surveyor (MGS; 1997-2006), Mars Express (MEX; 2004-present), and Mars Atmosphere and Volatile Evolution (MAVEN; 2014-present) missions have revealed major effects of the crustal fields on the Martian induced magnetosphere through various phenomena, such as plasma precipitation (Brain et al., 2007; Fang et al., 2010; Lillis & Brain, 2013) and induced auroras (Bertaux et al., 2005; Schneider et al., 2018), density depletions

21699402, 2022, 5, Downloaded from https://agupubs.onlinelibrary.wiley.com/doi/10.1029/2021JA030146 by Cochrane France, Wiley Online Library on [23/11/2022]. See the Terms and Conditions (https://onlinelibrary.wiley.com/terms-and-conditions) on Wiley Online Library for rules of use; OA articles are governed by the applicable Creative Commons License

21699402, 2022, 5, Downloaded from https://agupubs.onlinelibrary.wiley.com/doi/10.1029/2021JA030146 by Cochrane France, Wiley Online Library on [23/11/2022]. See the Terms and Conditions (https://onlinelibrary.wiley.com/terms-and-conditions) on Wiley Online Library for rules of use; OA articles are governed by the applicable Creative Commons License

(Hall, Lester, Nichols, et al., 2016; Mitchell et al., 2001; Steckiewicz et al., 2017), ion escape (Fang et al., 2010; Ma et al., 2014; Poppe et al., 2021; Romanelli et al., 2018), cross terminator transport (Fang et al., 2015; Xu et al., 2016), and magnetic reconnection in the tail region (DiBraccio et al., 2018).

The interaction between Mars and the solar wind results in several plasma boundaries, such as the bow shock (hereafter BS), the Induced Magnetospheric Boundary (IMB) or Magnetic Pile-Up Boundary (MPB), the Ion Composition Boundary (ICB), the PhotoElectron Boundary (PEB) or the ionopause. These boundaries are highly dynamic and depend on both internal and external drivers. Studying their dynamics is crucial to better understand the response of the Martian environment and thus its evolution with time. The SW dynamic pressure was considered a major driver for the BS and MPB location (Crider, 2004; Vignes et al., 2002). Edberg et al. (2010) showed that the magnetosonic Mach number of the SW also influences significantly the BS. Later, Hall, Lester, S´anchez-Cano, et al. (2016) analyzed MEX data and showed that the BS location is more sensitive to seasonal variations in the solar extreme ultraviolet (EUV) irradiance than to SW dynamic pressure variations, and Hall et al. (2019) also showed the influence of solar cycle EUV variations. Moreover, Halekas et al. (2017) showed the major influence of the magnetosonic Mach number and EUV, as well as a significant influence of SW dynamic pressure but a weak dependence on the geographical longitudes (which would have been expected due to non-uniformly distributed crustal fields).

Among the various drivers of the BS location, the crustal magnetic fields of the planet are among the least understood. Previous studies suggested an influence of the crustal fields, characterized by differences between the north and south locations of BS (e.g., Mazelle et al. [2004]), presumably attributed to the strongest crustal source region located in the southern hemisphere of the planet (centered on ∼− 45° IAU latitude and ∼180° IAU longitude). Such hemispheric differences were also observed for other boundaries (Garnier et al., 2017; Matsunaga et al., 2017). However, these comparisons showed a weak dependence on the position of the strongest crustal source region, with no clear longitude modulation found. Edberg et al. (2008) proposed wide (i.e., 120°) longitude bins exhibiting large differences in terms of BS location, these differences being found much smaller with MAVEN by Halekas et al. (2017). Gruesbeck et al. (2018) showed that the strongest crustal source region in the southern hemisphere had a different influence on the BS location depending on the dayside versus nightside location of the source region. Fang et al. (2017) (hereafter XF17) also suggested a rather global influence of the crustal field on the BS, and that the crustal magnetic pressures over different solar zenith angle zones exert different influences. Recently, Nemec et al. (2020) compared the influence of EUV, SW dynamic pressure, and local crustal field intensity on the MAVEN BS crossings, suggesting a non-negligible influence of local crustal fields but still much smaller compared to the other two drivers. Overall, the influence of the crustal fields on the BS is still under debate - from little influence (Edberg et al., 2009; Li et al., 2020) to strong variability, up to above 1,000 km altitude differences in the BS location based on North/South asymmetries (Edberg et al., 2008; Gruesbeck et al., 2018) - or in terms of local (Nemec et al., 2020) versus more global (Fang et al., 2017) spatial extent. For these reasons, the main goal of this study is to do the best-to-date characterization of the behavior of the Martian BS over crustal fields using all available datasets.

In this study, we analyze shock crossing datasets from both the MEX and MAVEN missions. We describe the data in Section 2.1 and our methods in Section 2.2. The results of our study are shown in Section 3, starting with a detailed analysis of the influence of the crustal fields on the Martian shock location in Section 3.1. Then Section 3.2 describes thepartial correlation approach to investigate existing biases versus Extreme UltraViolet fluxes and confirm the significance of the crustal field's influence on the shock location. We finally provide a discussion and conclusion in Sections 4 and 5.

2. Datasets and Methods

2.1. Description of the Datasets

We analyze the observations by two missions - MEX and MAVEN - to support the results obtained and avoid biases related to mission specificities.

We first used the list of MEX crossings derived by Hall, Lester, S´anchez-Cano, et al. (2016), in which an automatic algorithm is used to detect the BS crossings in the measurements from the MEX instrument Analyzer of Space Plasmas and Energetic Atoms (ASPERA-3) Electron Spectrometer (ELS). The ASPERA-3 ELS is an electron spectrometer able to detect electrons in the energy range of 1 eV–20 keV with an energy resolution of around

21699402, 2022, 5, Downloaded from https://agupubs.onlinelibrary.wiley.com/doi/10.1029/2021JA030146 by Cochrane France, Wiley Online Library on [23/11/2022]. See the Terms and Conditions (https://onlinelibrary.wiley.com/terms-and-conditions) on Wiley Online Library for rules of use; OA articles are governed by the applicable Creative Commons License

8% (Barabash et al. [2006]). From January 2004 to May 2015, 12,091 BS crossings were identified. Among these, we reduced multiple crossings occurring within a minute into one event, leading to 11,820 crossings in total for the MEX BS.

Two MAVEN studies dealing specifically with the analysis of the BS boundary - XF17 (who used the list published by Masunaga et al. [2017]) and Gruesbeck et al. (2018) - provided lists of 2934 and 1957 BS crossings over the periods November 2014 to March 2016 and November 2014 to March 2017, respectively. These crossings were identified based on the MAVEN MAG magnetic field data (Connerney et al., 2015), SWEA electron data (Mitchell et al., 2016), and SWIA ion data (Halekas et al., 2015). We removed the crossings that overlapped in time or occurred at the same time within an hour, reducing our MAVEN list to 3837 BS crossings.

A large number of BS crossings of MEX and MAVEN - thanks to their relatively short orbital periods of 6.7 and 4.5 hr, respectively, - provides a large spatial and temporal coverage for statistical analyses. The coverage in terms of solar EUV flux and SW dynamic pressure, known as significant drivers, is also sufficiently broad (see the dataset descriptions by Hall, Lester, S´anchez-Cano, et al. [2016b] and Masunaga et al. [2017]). However, a noteworthy difference exists between both datasets: MEX covers a whole solar cycle (2004-2015, with the solar maximum in 2014), while the MAVEN dataset corresponds to a shorter period (2014-2017) where the mean EUV level (given by the solar 10.7 cm radio flux) was larger by ∼14% at the time of the crossings compared with the MEX dataset. Since the absolute location of the BS may be different between both datasets due to solar activity variability (see Section 3.1), we thus focus on the variability of the BS location rather than on their absolute values.

Moreover, we use a third dataset based on the Mars Global Surveyor (MGS) mission data analysis by Vignes et al. (2002). MGS included a dual fluxgate magnetometer (MAG) and an electron reflectometer (ER; Acuña et al. [1992]). This third dataset contains 544 BS crossings occurring during the pre-mapping phase of the mission where the orbit was eccentric enough to cross the shock. However, this third dataset is considered with caution, since the number of crossings is limited compared to the MEX and MAVEN datasets. Furthermore, the dataset crossings occurred over a single year (from September 1997 to September 1998, after the solar minimum in 1996) when a relatively narrow range of EUV fluxes (three times smaller than MAVEN) and solar wind properties was covered.

Finally, we use in Section 4 Total Electronic Content ionospheric data from the MARSIS instrument onboard MEX. TEC retrievals are given from the planetary surface until MEX altitude and are obtained when MARSIS operates in the subsurface mode (see more at Sánchez-Cano et al. [2015]). The algorithm for the retrieval is described in Cartacci et al. (2013,2018). Only data with a signal-to-noise ratio >15 dB were used to remove noise and bad quality data.

2.2. Description of the Methods

2.2.1. The Extrapolated Terminator Altitude of the Shock

We use a one-dimensional approach to investigate the variability of the BS location, by considering the so-called extrapolated terminator altitude, defined as follows.

We first rotate (by 4°) the crossing locations into the SW aberrated cylindrical MSO system, to account for the aberration of the solar wind flow direction by the planetary orbital motion. The MSO frame (X,Y,Z) coordinates are defined as follows: X points toward the Sun, Y points approximately opposite to Mars orbital angular velocity and Z completes the right-handed set. We neglect the axis asymmetry of the BS (see Fang et al. (2015)) and assume the shock boundary can be fitted by a conic section described by the following equation:

$$r = \frac{L}{1 + e\cos(\theta)} \quad (1)$$

where r is the distance to the focus located at (X0, 0, 0), L and e are respectively the semi-latus rectum and eccentricity. As performed by previous authors (see e.g., Edberg et al., 2008 or Hall, Lester, S´anchez-Cano, et al., 2016), we calculate the extrapolated terminator altitude, defined by the altitude of the conic in the aberrated terminator plane:

$$R_{TD} = \sqrt{L^2 + (e^2 - 1) \cdot X_0^2 + 2 \cdot e \cdot L \cdot X_0} - R_M \quad (2)$$

where RM is the Martian radius (3,390 km). This parameter represents the variability of the BS location, removing the strong solar zenith angle influence by projecting the crossing point toward the aberrated terminator along an assumed conic fit. This simple procedure prevents doing complex analysis of 3D asymmetries as done by Gruesbeck et al. (2018) but is efficient to focus on a single parameter influence (e.g., the crustal fields). We used the L and e values published by Hall et al. (2016b) for the MEX crossings ($L = 1.82$ RM, $e = 1.01$), and the values published by XF17 for MAVEN ($L = 2.303$ RM, $e = 0.872$). Note the impact of using various data sets and conic fit parameters is discussed further in Section 3.2.

Note that we could wonder whether a one-dimensional approach, that projects the crossing point along a conic fit, is appropriate to investigate local variabilities of the shock location such as induced by crustal fields. However, first, the magnetosonic waves do not propagate radially only, the impact of crustal fields after magnetosonic wave propagation upstream of the planet will thus necessarily influence the shock location in a rather wide region given the distance of the shock. Second, if the influence was very localized at the shock location, this would have been observed earlier and is in contradiction with the large extent of the influence shown in the following sections, which confirms the ability of the one-dimensional approach to study the crustal field influence.

2.3. Statistical Tools

Beyond the direct analysis of the extrapolated terminator altitude, we use in this paper correlation approaches defined below: linear Pearson correlation coefficients, unpaired *t*-tests, and partial correlations.

First, simple correlation factors are analyzed in Sections 3.1 and 3.2. By default, we consider in the paper Pearson correlation coefficients that inform us about the strength and direction of the linear relationship between two variables, with values ranging from −1 (perfect anti-correlation) to +1 (perfect correlation).

In order to evaluate the significance of the correlation factor which strongly depends on the sample size, we make statistical tests. A *t*-test evaluates the test statistics associated with the correlation and compares it with a threshold defined for a given risk. This threshold corresponds to the statistics of the null hypothesis H0, which is the hypothesis of no significant correlation. The correlation is considered significant if the test statistics t is above the threshold, otherwise, the correlation factor is not considered significant with sufficient confidence. The risk value chosen by default for calculating the threshold is 5%, corresponding to a 2 standard deviations (i.e., 95%) tolerance interval for a gaussian probability distribution. Alternatively, two-sided p-values can be calculated to provide the probability that the null hypothesis is true. If the p-value is larger than the risk limit assumed (5% here), there is insufficient confidence that a significant linear relationship exists. On the other hand, if the p-value is smaller than the limit risk considered, the null hypothesis is rejected and the correlation is considered significant. In the rest of the study, we will mention that p-values are negligible when they are smaller than 10^{-5} and note them with "(n)".

Unpaired *t*-tests are also used in Section 3.2. These procedures compare two independent groups to determine if there is a significant difference between them. They assess whether the two groups have significantly different mean values. p-Values can also be associated with these tests as for correlation tests.

Beyond these well known methods - linear Pearson correlation coefficients and unpaired *t*-tests -, we use a partial correlation approach in Section 3.2 to mitigate possible biases due to cross correlations between drivers. The partial correlation approach (Baba et al., 2004; see Appendix A for a detailed description of the method) identifies individual relationships among variables that may be correlated, and calculates the correlation coefficients - and estimates their significance - between two variables after controlling for the influence of other variables. This technique is not a common tool in the literature, but it has been successfully used by several authors in studies such as the solar wind Earth interaction (Kim et al. (2011); Simms et al. (2021)), solar physics (Le & Zhang, 2017; Trottet et al., 2015), surface planetology (Anderson &Bell, 2013) and galaxies and compact objects (Dai et al., 2018; Kang et al., 2018; Ni et al., 2020; Yesuf & Ho, 2019).

For example, if one considers only three variables that are possibly correlated (x, y, z), the partial correlation between x and y, after controlling for z, is calculated as follows: first the linear regression between x and z is

21699402, 2022, 5, Downloaded from https://agupubs.onlinelibrary.wiley.com/doi/10.1029/2021JA030146 by Cochrane France, Wiley Online Library on [23/11/2022]. See the Terms and Conditions (https://onlinelibrary.wiley.com/terms-and-conditions) on Wiley Online Library for rules of use; OA articles are governed by the applicable Creative Commons License

21699402, 2022, 5, Downloaded from https://agupubs.onlinelibrary.wiley.com/doi/10.1029/2021JA030146 by Cochrane France, Wiley Online Library on [23/11/2022]. See the Terms and Conditions (https://onlinelibrary.wiley.com/terms-and-conditions) on Wiley Online Library for rules of use; OA articles are governed by the applicable Creative Commons License

performed, and the residuals are given by the difference between the x values and the regression. Subtracting the regression line removes the linear influence of z on x. Residuals are then calculated for y with the same procedure to remove the linear influence of z on y. The partial correlation coefficient between x and y, after controlling for the third variable z, is simply determined by the Pearson correlation coefficient between these two residuals. This technique can be generalized to a larger number of variables.

The relations are assumed linear with this technique ($y = a + \sum_i x_i \cdot b_i$ with a intercept and b_i slopes), but can also correspond to power law relations (of the type $y = a \prod_i x_i^{b_i}$) when linearized with a logarithm. As for direct correlations, the linear assumption is actually a weak assumption and does not need linear relationships between the parameters to remain valid, since the linear assumption keeps true in first order in most cases. In order to evaluate the significance of the partial correlation factors, as for zero-order correlations, a *t*-test can be performed to evaluate the test statistics that shall be larger than the threshold associated with the null hypothesis H0, and p-values provide the probability that the null hypothesis is true (i.e., that there is no significant partial correlation).

In the rest of the paper, correlations factors and significance test statistics and p-values by default correspond to direct linear correlations, the use of the partial correlations is explicitly specified.

3. Results

3.1. The Influence of Crustal Fields: Local Versus Global Influence

Several authors attempted to analyze the influence of the crustal fields on the BS location. The first obvious way is to consider correlations with the geographical longitude, to uncover the influence of the strongest crustal source region located in the southern hemisphere at ∼ [150,230]° East longitude and in the ∼ [−90 0]° latitude range (see the crustal field map in Figure 3d). Edberg et al. (2008) used this approach for MEX but could only obtain a rough trimodal behavior with three wide (i.e., 120°) longitude bands with different BS distances attributed to the influence on the crustal source. Nevertheless, as cautioned by XF17, the longitudinal position provides only partial but not full information on the orientation of the strongest crustal field region with respect to the impinging solar wind, the latter of which is critical for determining the bow shock formation and location. Overall, most authors essentially attributed the presence of a hemispheric asymmetry to crustal fields (Gruesbeck et al., 2018; Mazelle et al., 2004). On the other side, Nemec et al. (2020) recently quantified the dependence of the stand-off distance of the Martian BS with respect to local crustal fields, using the local crustal field at 400 km altitude from the Morschhauser et al. (2014) model, to show their influence is non-negligible but much smaller than EUV or SW dynamic pressure.

We also performed a direct longitude dependence analysis using the MEX and MAVEN datasets (not shown here), showing no clear dependence except by selecting large longitude bands as performed by Edberg et al. (2008). However, one can refine the analysis by considering only a (±20°) latitude band around the strongest crustal source region located around ∼ − 45° latitude and ∼180° longitude. This leads to focus on a latitude band with a highly variable crustal field intensity around the planet (see Figure 3d where the latitude band limits are superimposed on the crustal field map). The result is shown in Figure 1 for the three datasets (MAVEN, MEX, and MGS). A pattern with a "smile" shape is suggested and is roughly consistent among the three missions, with a minimum BS terminator altitude R_{TD} at small/large longitudes (corresponding to weak crustal field regions, see the colorbar) and a maximum value near ∼180° East longitude where the strongest crustal source region is located. The MEX median profile (and the percentiles area) shows a clear modulation with a minimum in the range 270°–20° (the two strongest minima of crustal fields being located close to 270–280° and around 360/0°). The MAVEN median curve is flatter except a clear peak at 180–225° and a low point at 360/0°, but the small dips of MAVEN seem close to crustal field intensity gaps. The MGS median curve is noisy, but overall also consistent with a "smile" shape.

Moreover, taking the terminator altitude versus the cosine of the longitude (translated into the range −180° to 180°) leads to correlation coefficients of −0.10 and −0.11 for MAVEN and MEX. The correlation is negative since the strongest crustal source region is centered on cos(longitude) = −1 while larger cosine values correspond to regions farther from the strongest crustal source region. These correlations may seem small but are still statistically significant given a large number of points, with p-values of about $4{\cdot}10^{-3}$/$2{\cdot}10^{-8}$, respectively, for MAVEN/MEX, that is, far below the 5% commonly considered as an acceptable value. In absolute values, the average BS

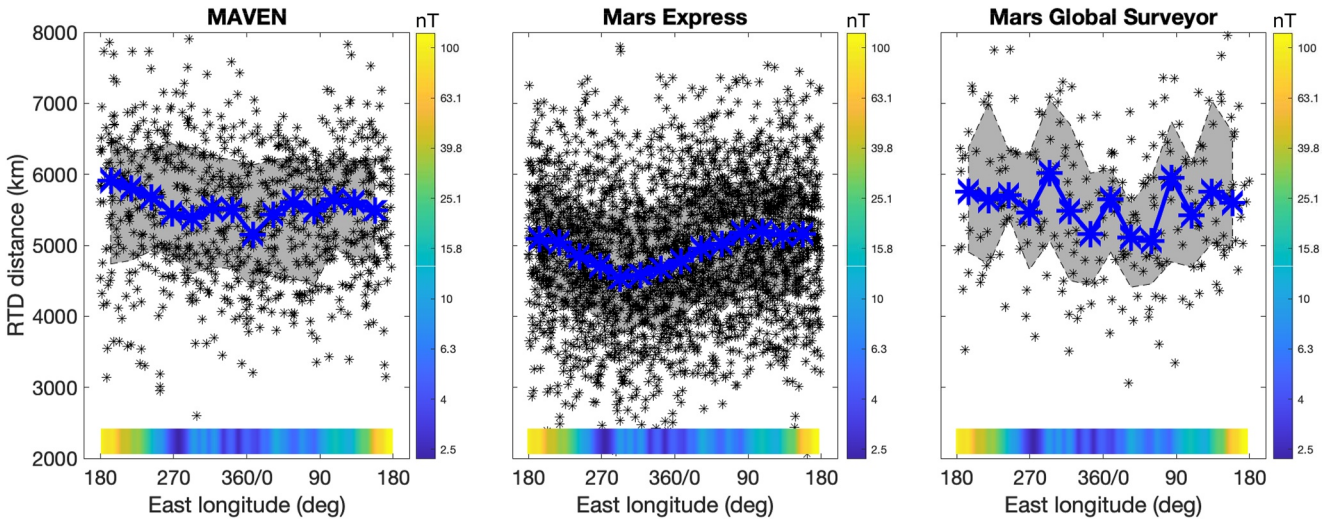


Figure 1. Geographical longitude modulation of the shock terminator altitude for all crossings (points) or the median profile (line), for the shock datasets from Mars Atmosphere and Volatile Evolution (left panel), Mars Express (middle panel), and Mars Global Surveyor (right panel). Only crossings that occurred at latitudes inside a ±20° latitude band around the strongest crustal source region (assumed centered around ∼−45° latitude and ∼180° longitude) were considered. The shaded area covers the 20%–80% percentiles range of shock terminator altitudes. The colorbar shows the longitude modulation of the crustal magnetic field intensity (logarithmic scale, in nT) from the Morschhauser et al. (2014) model at 400 km altitude, averaged over 1° longitude bins in the ±20° latitude band.

altitude decreases by 300 km (290/310 km for MAVEN/MEX) from the longitude sector (135–225° East longitude) of the strongest crustal source region to sectors away from it.

The correlation for the MGS dataset is also negative (∼−0.12, with a p-value of 0.04) but is closer to the significance limit due to the lower number of data. Due to the relatively low number of events and smaller significance, we mostly focus on the MEX and MAVEN datasets in the rest of the study, and only briefly mention the MGS data analysis to discuss the consistency among the mission observations.

We further investigate whether the crustal field influence is global or local. We calculated the correlation between the terminator altitude and either the angular averaged pressure of the crustal magnetic field $B^2/(2_{\mu_0})$ or the angular averaged crustal magnetic field magnitude. B is the crustal magnetic field magnitude at 400 km altitude from Morschhauser et al. (2014) averaged over an area defined by a variable angular range around the sub-spacecraft location of the spacecraft: for example, 40° range means we average the crustal field pressure or the crustal field intensity over an angular range (based on spherical distance calculations) of 40° around the exact longitude/latitude of the crossing, while 0° means we consider the pressure at the exact longitude/latitude of the crossing (i.e., the local value with no averaging). Such analysis, shown in Figure 2, reveals a positive correlation for both MAVEN/MEX increasing until a maximum of 70–80° angular range. The correlation for MAVEN/MEX with the crustal pressure rises from 0.04/0.11 at 0° to 0.18/0.33 at 70–80° angular range (with statistically significant correlations even for 0° angular range and negligible p-value at maximum correlation). Similar peak correlations (even slightly larger for MAVEN) are observed when considering the crustal field intensity instead of the pressure, but the profile becomes more flat with a less pronounced peak. Note that using an even smaller power law index for the crustal field intensity, such as $\left(B^2/(2\mu_0)\right)^{1/6}$ as used by XF17, also leads to similar results with close peak correlation factor values and an even more flat profile (more and more flat when smaller power law index values of the pressure are considered). The correlation between the terminator altitude of the BS and the crustal fields (either the pressure, or powers law values of it) is always significant but maximizes for a large angular range considered. Our results suggest a rather global influence (slightly less than hemispheric) of the crustal field pressure on the BS location, in closer agreement with the finding by XF17 rather than the approach considered by Nemec et al. (2020).

We also convolved the crustal field pressure with an angular Gaussian filter (with a variable standard deviation σ defined dynamically) to evaluate the influence of the crustal fields at the sub-spacecraft location compared to farther longitudes/latitudes, leading to similar maximum correlation values for $\sigma > 60°$ (not shown). The need for large angular ranges is expected based on the large distance of the BS boundary and is in agreement with previous

21699402, 2022, 5, Downloaded from https://agupubs.onlinelibrary.wiley.com/doi/10.1029/2021JA030146 by Cochrane France, Wiley Online Library on [23/11/2022]. See the Terms and Conditions (https://onlinelibrary.wiley.com/terms-and-conditions) on Wiley Online Library for rules of use; OA articles are governed by the applicable Creative Commons License

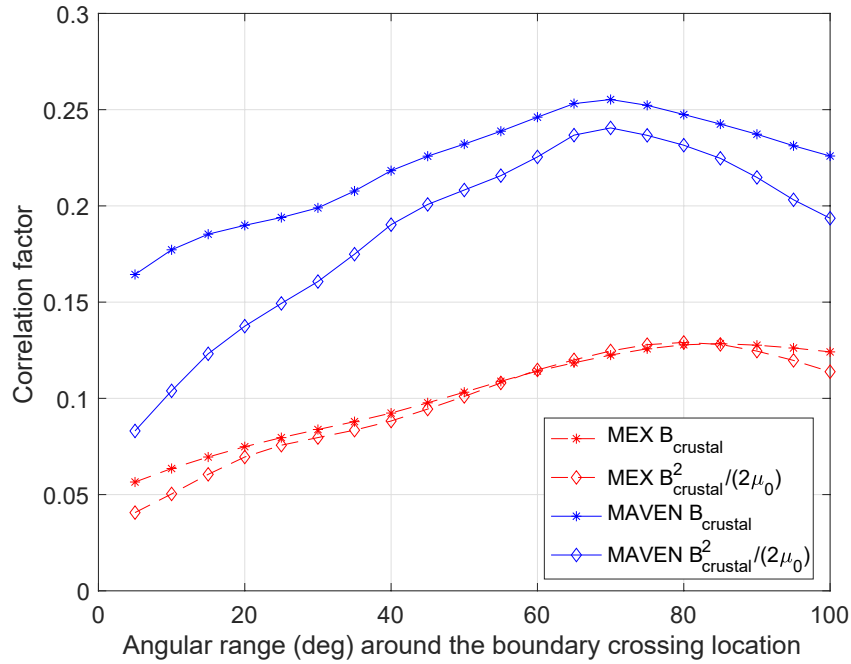


Figure 2. Correlation factor between the R_{TD} terminator altitude of the shock crossings (for Mars Atmosphere and Volatile Evolution in blue, for Mars Express in red) and crustal magnetic field pressure or intensity. The crustal field magnetic field intensity or pressure are taken from the Morschhauser et al. (2014) model at 400 km altitude at the sub-spacecraft position (same IAU longitude and latitude) below the crossing, then averaged over an angular range around the sub-spacecraft location. The correlation factor is given as a function this angular range, to reveal whether the crustal field influence on the shock location is local or global.

studies showing a rather global influence. Note that the MGS BS dataset also suggests an increasing correlation between the BS distance and the angular range (with a peak at 110° and a maximum correlation factor of 0.4). Any functional forms of the BS location variability with respect to the crustal fields thus need to consider the large-scale effect of the crustal fields rather than a local effect: the small power law index value (0.018) associated with the local crustal field pressure influence on the Martian BS location by Nemec et al. (2020) thus inevitably underestimated the crustal field effects due to the limitation of using only local crustal field distributions.

Figure 3 provides another examination of the local versus the global influence of the crustal fields on the BS location. It shows the logarithmic value of the occurrence frequency of the MAVEN/MEX BS crossings as a function of the terminator altitude and of the angular distance from the strongest crustal source region (assumed at ∼−45° latitude and ∼180° East longitude, see Figure 3d). The angular distance is the angle between the planetary center - spacecraft vector and the planetary center - strongest crustal source region center vector. The occurrence frequency is simply the number of shock crossings counted in each cell of the two dimensional grid defined by the angular distance and the terminator altitude, then given in % of the total number of crossings. We use the angular distance to consider that the crustal field may influence the plasma environment and thus the BS boundary in any direction, not only along the longitude.

Both MAVEN/MEX results (Figures 3a and 3b) are very similar and reveal a dominant influence of the strongest crustal field region, with the BS altitude decreasing farther from it. The error bars of the distribution is large probably due to the presence of all other parameters of influence (SW pressure, solar EUV…). The mean altitude is larger in the 0–80/90° angular distance range than beyond, which is consistent with the maximum correlation for the 70–80° angular range as seen in Figure 2. However, a plateau appears in both datasets in a narrower angular range 0–40/60° which is consistent with a dominant influence of the strongest crustal field region whose angular extent is of the same order of magnitude (see Figure 3d). On top of the major trend, we notice a slight lift in the BS altitude in the ∼110–140° angular distance range, which could be attributed to the strong secondary crustal field sources located at such angular distances near the equator (see same panel). The trend in the MAVEN dataset is

21699402, 2022, 5, Downloaded from https://agupubs.onlinelibrary.wiley.com/doi/10.1029/2021JA030146 by Cochrane France, Wiley Online Library on [23/11/2022]. See the Terms and Conditions (https://onlinelibrary.wiley.com/terms-and-conditions) on Wiley Online Library for rules of use; OA articles are governed by the applicable Creative Commons License

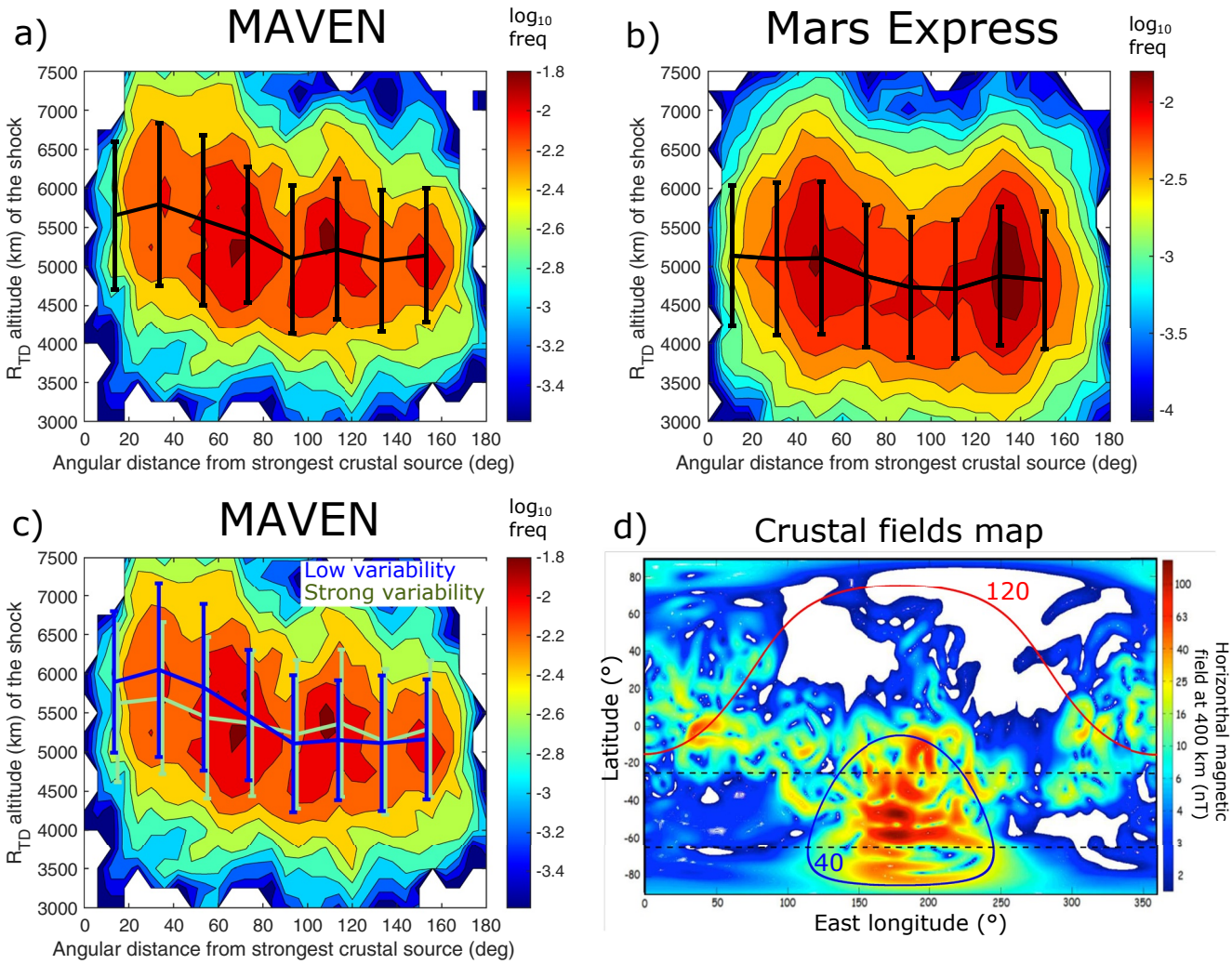


Figure 3. Logarithmic occurrence frequency of the shock crossings distributions for the Mars Atmosphere and Volatile Evolution (panel a and c) and Mars Express (panel b) datasets as a function of the terminator altitude and of the angular distance from the strongest crustal source region center (see text for details). The mean and standard deviation are superimposed. Panel (c) same distribution as panel a, with means and standard deviations for either low or strong IMF clock angle orientation variabilities preceding the BS crossings. Panel (d) geographical map of the horizontal crustal magnetic field at 400 km altitude, with isocontours of the angular distance from the strongest crustal source region (blue line for 40°, red line for 120°) and two isolatitude lines at −25° and −65°.

more prominent than in the MEX dataset, which will be discussed later. Moreover, despite a poorer coverage, the MGS dataset also shows a decrease in the BS distance with angular distance.

One of the challenges of disentangling the crustal field influence is the presence of many other driving factors, including the dynamics of the incident SW and IMF. Indeed, the crustal fields act as pressure enhancements, induce currents that propagate into the Martian plasma environment, through a complex interplay between the incident magnetosheath plasma transport and the magnetic field topology arising from the draping of the Interplanetary Magnetic Field (IMF) around the planet and modified by the planetary crustal fields themselves. The whole interaction is driven by the SW plasma and magnetic field, whose orientation varies with time. When the IMF rotates at short timescales, the influence of the crustal fields, which is essentially a geographical influence in the planetary frame with a larger timescale, may be partially masked due to the rotation of the interaction. Several external or internal drivers control the BS location, but the IMF rotation may partially hide the geographical influences such as crustal fields.

Figure 3c shows the same MAVEN map as Figure 3a, but we superimposed mean values during the periods of low and high IMF clock angle variabilities. The IMF clock angle was calculated from the upstream conditions

21699402, 2022, 5, Downloaded from https://agupubs.onlinelibrary.wiley.com/doi/10.1029/2021JA030146 by Cochrane France, Wiley Online Library on [23/11/2022]. See the Terms and Conditions (https://onlinelibrary.wiley.com/terms-and-conditions) on Wiley Online Library for rules of use; OA articles are governed by the applicable Creative Commons License

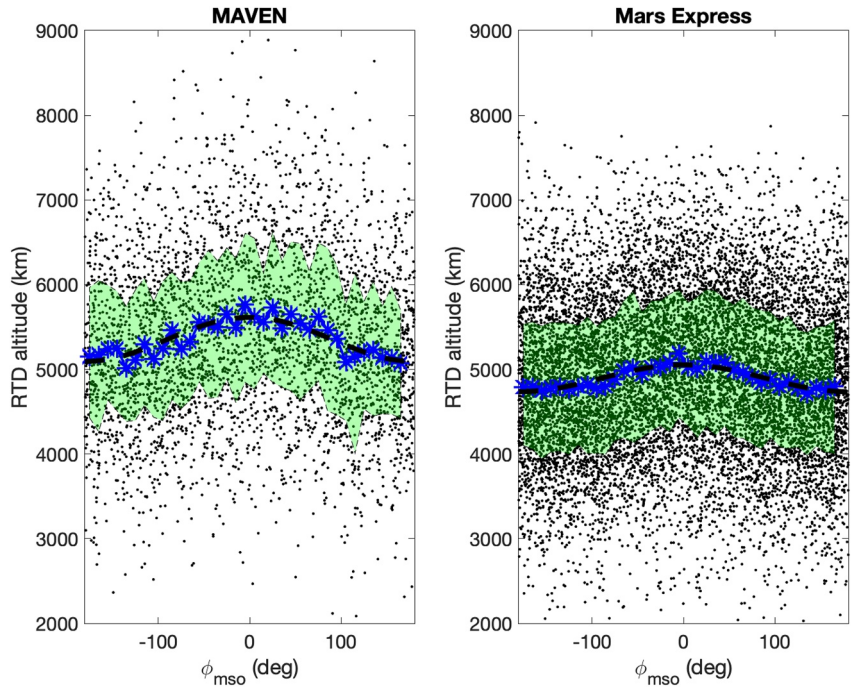


Figure 4. Mars Atmosphere and Volatile Evolution (left) and Mars Express (right) shock R_{TD} terminator altitude as a function of ϕ_{mso} the MSO longitude of the strongest crustal source region center: 0° at noon, +90° at dusk −90° at dawn. The mean observed profile (blue stars) is compared with a simple cosine fitting (black dashed line). The shaded area covers the 20%–80% percentiles range of shock terminator altitudes.

prior to the BS crossings, defined as $\tan^{-1}\left(B_{Z_{IMF}}/B_{Y_{IMF}}\right)$. We use the standard deviation of the clock angle over the 2 hrs before the crossings as a measure of the rotation dynamics of the IMF, and divide the whole MAVEN dataset into one low (i.e., below the median standard deviation value) and one high (i.e., above the median standard deviation value) variability dataset. Panel c shows the mean R_{TD} of the BS for both sub-samples. As expected, the crustal field influence is less visible under high IMF clock angle variability conditions than under the low variability conditions, where the altitude difference is as high as up to 1,000 km.

The dynamics of the IMF can actually impact the BS at several levels that should be further analyzed in the future. In particular, a constant IMF or a sudden change of IMF to the same strength and orientation may have different effects on the BS locations. Depending on the conditions considered, the BS shape can be modified, with asymmetries of the global shape appearing, or a sudden compression followed by a recovery phase depending on the Mach number and on the dynamic pressure. Previous studies on Earth or Venus also suggested that a rotation of the IMF could have different consequences whether the local conditions lead to perpendicular or parallel shocks with higher perpendicular BS locations particular in the tail (Wang et al., 2016). At Venus or Mars authors suggested asymmetries of the BS location depending on the orientation of the $\overrightarrow{E} = -\overrightarrow{V} X \overrightarrow{B}$ electric field that increases the mass loading due to accelerated pickup ions (Alexander et al., 1986; Vignes et al., 2002).

We performed another correlation analysis between the BS terminator altitude and the crustal fields, by including a maximum threshold on the crustal field intensities (local values at 400 km altitude) considered in the analysis. The results show that no significant correlation between local crustal field intensities and the BS location appears as long as only intensities below a few nT are considered. The correlation then rises when the threshold increases to include stronger and stronger sources. This shows that even when considering only local crustal fields instead of angular averaged values, a large number of regions around the planet (intensities of few nT are observed in many regions) can influence the BS location beyond the southern hemisphere's strongest crustal source region. Nonetheless, the large size and strong intensity of the crustal fields in this region make it the major crustal field region driver.

Gruesbeck et al. (2018) also showed a significant influence of the local time of the strongest crustal source region on the 3D shape of the BS when it was located on the dayside versus on the nightside. Figure 4 shows how the

21699402, 2022, 5, Downloaded from https://agupubs.onlinelibrary.wiley.com/doi/10.1029/2021JA030146 by Cochrane France, Wiley Online Library on [23/11/2022]. See the Terms and Conditions (https://onlinelibrary.wiley.com/terms-and-conditions) on Wiley Online Library for rules of use; OA articles are governed by the applicable Creative Commons License

location of the strongest crustal source region impacts the BS distance using both MAVEN and MEX datasets. Despite large data scattering - with a standard deviation of ∼1,000 km - due to the combined effects of other driving factors, the average BS R_{TD} altitude is modulated by the MSO longitude (hereafter ϕ_{mso}, equivalent to local time) of the strongest crustal field region: the BS standoff distance peaks when the strongest crustal field region is located at noon. A similar trend may also be seen with the MGS dataset with clear peak at noon longitude. The mean profile suggests a reduced and steady or inexistent influence of the strongest crustal source region when it is located on the nightside.

These results thus suggest a dominant (but not unique) influence of the strongest crustal field region (with a large angular extent consistent with its size) on the BS location. This influence depends on the stability of the IMF orientation that may partially hide the crustal field influence, as well as on the local time of the strongest crustal source region. Regarding the latter, the information corresponding to the increased crustal field pressure by the strongest crustal source region rotation propagates upward at the fast magnetosonic wave velocity, and then probably impacts the location of the BS. The information reaches the solar wind flow faster at noon on the dayside than on the nightside due not only to the closer distance, but also to the fact that the magnetosonic waves from the nightside are partially attenuated, and the dayside fast mode magnetosonic wave speed is expected to be larger due to the increased magnetic field in the draping region. Consequently, enhanced crustal fields impact the BS surface, which is significantly reduced when the strongest crustal source region is located far from the noon direction. Figures 3 and 4 show that the crustal field can enhance the extrapolated terminator altitude of the Martian BS by several hundreds of km on average. This is in agreement with the large possible range mentioned in the literature, ranging from no or little influence (with e.g., about 100 km influence from MEX observations (Edberg et al. [2009] or simple dipole based MHD simulations; Li et al. [2020]) to ∼400 km altitude fluctuation according to XF17, and even above 1,000 km influence based on North versus South asymmetries (Edberg et al., 2008; Gruesbeck et al., 2018).

3.2. Investigating Statistical Biases

The previous section shows strong evidences regarding the influence of the crustal fields on the distance of the Martian BS, through several spacecraft and several methods providing consistent results: geographical longitude modulation, correlation versus crustal field pressure with a variable angular range, direct plotting of the distance versus the angular distance from the strongest crustal source region, location of the strongest crustal source region with respect to noon. However, differences arise between MAVEN and MEX, with higher absolute BS distances and an apparently stronger influence of the angular distance from the strongest crustal field region for MAVEN than for MEX.

The MAVEN and MEX datasets used in this study cover different periods (respectively 2014-2017 and 2004-2015), corresponding to different EUV conditions. The large MEX dataset provides a wide range of EUV conditions, with a full solar cycle (including the lower and extended ever recorded solar minimum), while the MAVEN dataset corresponds to a period with an active Sun in 2014 and 2015 (where most of our MAVEN crossings occurred) below a declining activity in 2016-2017. The mean EUV level of the MAVEN crossings (given by the solar 10.7 cm radio flux) was thus larger by ∼14% compared with the MEX dataset. The larger EUV conditions associated with the MAVEN dataset certainly contribute to the larger BS distances observed (by ∼5%) for MAVEN than for MEX. The EUV fluxes increase indeed the ionospheric scale height and the ionization rate of the Martian atmosphere, which adds mass to the solar wind flow through pickup ions and slows down the solar wind, then creating a larger apparent obstacle that pushes the BS further. The compared magnetosonic Mach number conditions, which also have a major influence on the BS location through the Mach cone conditions, may also have induced this absolute difference in the BS altitude between both missions, however, these conditions are not known precisely for the pre-MAVEN period.

A dedicated analysis also reveals a significant bias in the MAVEN dataset due to the EUV conditions during the BS crossings. Figure 5 provides the EUV values and occurrence frequency versus either the angular distance from the strongest crustal source region center or its MSO longitude for both missions. The EUV values were determined for MAVEN from the FISM model (Chamberlin et al. [2007]; available for MAVEN but not MEX) for 10–120 nm wavelengths, and for MEX from the solar 10.7 cm, radio flux index extrapolated to Mars assuming a $1/r^2_{Mars\,Sun}$ law. Using solar radio flux values for MAVEN leads to almost identical results since both parameters are strongly correlated (with a correlation factor of 0.98 (n)). However, we choose the FISM model for MAVEN

21699402, 2022, 5, Downloaded from https://agupubs.onlinelibrary.wiley.com/doi/10.1029/2021JA030146 by Cochrane France, Wiley Online Library on [23/11/2022]. See the Terms and Conditions (https://onlinelibrary.wiley.com/terms-and-conditions) on Wiley Online Library for rules of use; OA articles are governed by the applicable Creative Commons License

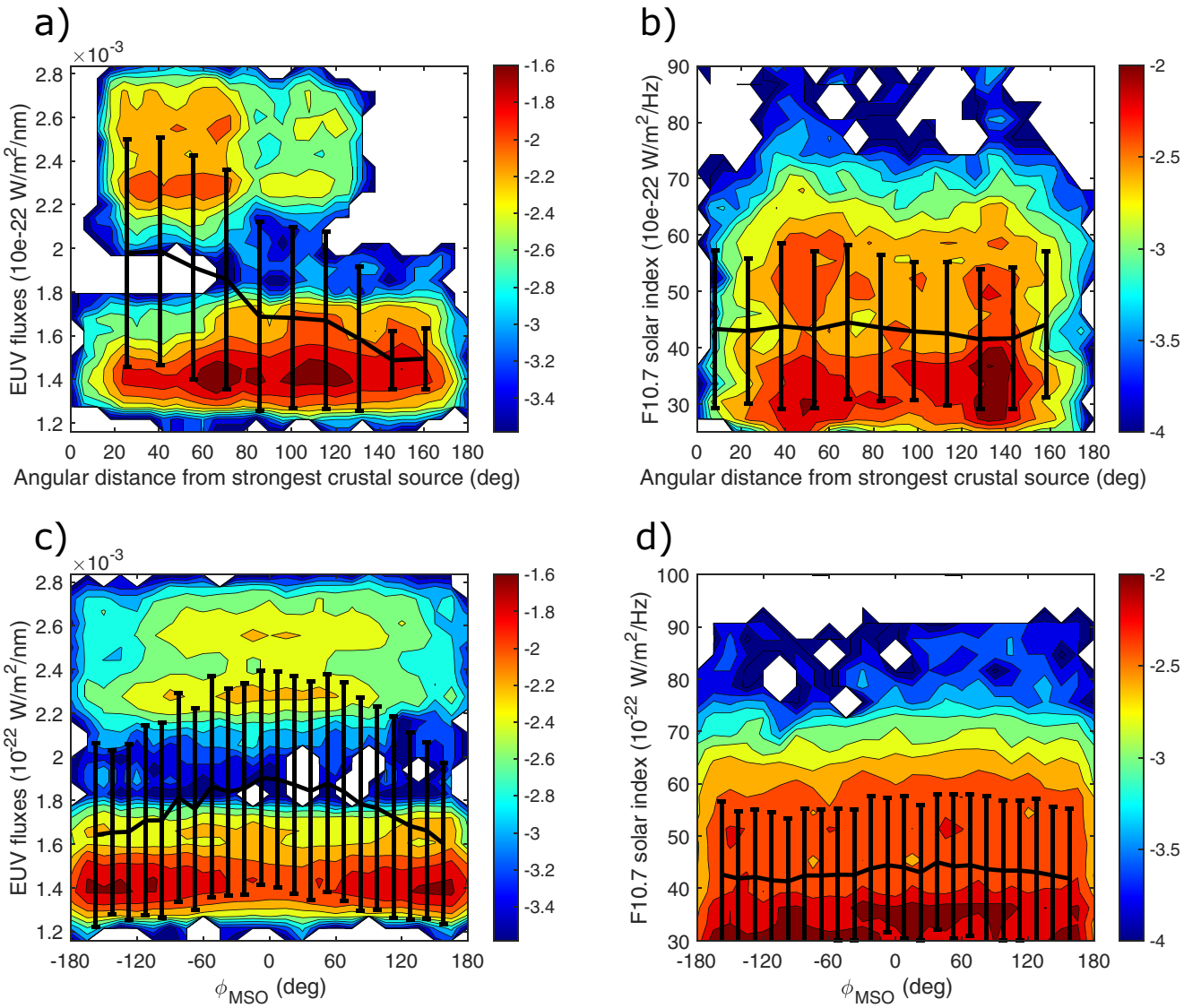


Figure 5. Logarithmic occurrence frequency of the shock crossings distributions for the Mars Atmosphere and Volatile Evolution (MAVEN) (left panels a and c) and Mars Express (right panels b and d) datasets as a function of the extreme ultraviolet fluxes (given by the FISM extreme ultraviolet fluxes for MAVEN and by the solar 10.7 cm radio flux index extrapolated to Mars for Mars Express) and of 1) either the angular distance from the strongest crustal source region (upper panels a and b) 2) or ϕ_{mso} the MSO longitude of the strongest crustal source region (lower panels c and d). The mean and standard deviation are superimposed.

since it is slightly more precise than the radio flux proxy (FISM uses data and a number of proxies including the radio flux proxy, to select the most appropriate information for each wavelength at each time). Moreover, the absolute values of EUV are of no interest in our case since we only focus on variabilities and correlations.

Figure 5b shows a MEX EUV distribution that is roughly uniform with regards to the angular distance from the strongest crustal source region or to ϕ_{mso}, with also more frequent low EUV fluxes than high fluxes. In contrast, the MAVEN EUV distribution (Figure 5a) reveals the presence of two separate regimes, one low and one high regime (with a difference of almost a factor of 2), corresponding to time periods before (high EUV fluxes) and after (low EUV fluxes) spring 2015. Moreover, the low MAVEN EUV fluxes mainly occurred when the spacecraft was away from the strongest crustal source region, while high EUV fluxes occurred close to the strongest crustal source region. Consequently, the EUV mean profile versus the angular distance to the strongest crustal source region is similar to the MAVEN mean profile of the BS distance (in Figure 3a). The interpretation of the crustal field influence on the BS distance from Figure 3 may thus be biased by the inhomogeneous EUV distribution induced by the evolution of the orbit of the spacecraft while the Sun activity decreased from 2014 to 2017. A

21699402, 2022, 5, Downloaded from https://agupubs.onlinelibrary.wiley.com/doi/10.1029/2021JA030146 by Cochrane France, Wiley Online Library on [23/11/2022]. See the Terms and Conditions (https://onlinelibrary.wiley.com/terms-and-conditions) on Wiley Online Library for rules of use; OA articles are governed by the applicable Creative Commons License

21699402, 2022, 5, Downloaded from https://agupubs.onlinelibrary.wiley.com/doi/10.1029/2021JA030146 by Cochrane France, Wiley Online Library on [23/11/2022]. See the Terms and Conditions (https://onlinelibrary.wiley.com/terms-and-conditions) on Wiley Online Library for rules of use; OA articles are governed by the applicable Creative Commons License

similar bias also appears regarding the EUV profile versus ϕ_{mso} (panels c vs. d), with a clear peak at noon similar to the peak observed for the MAVEN BS location in Figure 4. Both biases are related to the orbital precession of the MAVEN spacecraft. These biases may then increase artificially the apparent influence of crustal fields in the MAVEN data analysis that appeared stronger than in the MEX case.

These biases may also be seen through the linear Pearson correlation factors, on one side, between the angular distance and the BS extrapolated terminator altitude, and on the other side between the angular distance and the main controlling parameters of the BS drivers that are a priori the EUV fluxes and magnetosonic mach number (Halekas et al., 2017). The MAVEN magnetosonic mach number (Mms) is calculated with the method by Halekas et al. (2017): $Mms = v_{sw}/\sqrt{c_s^2 + v_A^2}$, with v_{sw} SW speed, c_s sound speed, v_A Alfvén speed, with the electron temperature assumed equal to the proton temperature and a polytropic index $\gamma = 5/3$. It cannot be calculated for MEX due to the lack of magnetic field measurements.

The linear correlation coefficients show indeed that the angular distance is more correlated with EUV fluxes for MAVEN (correlation factor −0.34 (n)) than it is with the BS terminator altitude R_{TD} (correlation factor of −0.24 (n)). The same comparison can be done for ϕ_{mso} and its correlation with EUV (correlation factor 0.21 (n)) compared to R_{TD} (correlation factor 0.19 (n)). The situation for MEX is the contrary, thus confirming the absence of bias in the MEX case. We note that the Mms do not introduce a significant bias, with for MAVEN small correlations between the angular distance and the Mms (correlation factor of 0.04 with a large p-value above 1%) compared to the correlation between angular distance and R_{TD}.

As a consequence, a part of the MAVEN observed dependence of the BS distance on the angular distance or the MSO longitude of the strongest crustal source region is probably due to the cross-correlations of these parameters with EUV (see below the partial correlation analysis for a better understanding of the influence of this cross-correlation). These biases may have influenced the results obtained by Gruesbeck et al. (2018) who showed strong hemispheric differences in their 3D modeled BS, either regarding the North/South difference or when the strongest crustal source region was on the dayside versus nightside. More precisely, when focusing on low Solar Zenith Angles (SZAs) in their study, the EUV fluxes were indeed maximum for low SZAs of the spacecraft and in the southern hemisphere, leading to a strong north/south asymmetry (>1,000 km) that was only partially caused by the presence of crustal fields. Moreover, we shall add that using the North versus South asymmetries and attributing them to the crustal field influence (as performed in a number of studies of the Martian interaction) may be significantly biased by the seasonal change of EUV fluxes sweeping between the northern and southern hemispheres during the summer and winter solstices. The North versus South asymmetry caused by crustal fields may thus be overestimated or underestimated depending on the seasons due to the significant influence of EUV-induced ionization. At high (solar EUV) illumination periods of the Martian orbit, one can even observe BS on average further in the northern hemisphere than in the southern hemisphere.

However, these biases impact only the influence of the angular distance and the MSO longitude to the strongest crustal source region in the case of the MAVEN dataset. They impact neither the MEX dataset nor the analysis of Figure 1 for the MAVEN dataset: there is no correlation between the IAU longitude and the EUV, with a large p-value (35%) when testing for the linear correlation between the cosine of the IAU longitude and the EUV (when selecting only the latitudes around the strongest crustal source region).

In order to confirm that the influence of the angular distance to the strongest crustal source region or of its ϕ_{mso} is not due only to the EUV influence in the MAVEN case, we performed a partial correlation analysis. An approach based on subsets of the whole dataset was tried at first, by separating low versus strong EUV conditions subsets to remove its major influence, but this leads to poor coverage of the crustal fields (in angular distance or crustal field pressure) and can thus not be used to identify the influence of crustal fields.

Table 1 provides the results for a partial correlation analysis of the influence of angular distance and the cosine of ϕ_{mso} on the extrapolated terminator BS altitude (R_{TD}), after controlling the other main parameters of influence. We here consider as controlling parameters the EUV fluxes (for MAVEN/MEX) and magnetosonic Mach number (for MAVEN only) which are known major parameters of the influence of the BS location.

The partial correlation analysis makes it possible to compare the correlation factors between two variables before and after controlling for the other considered parameters. In the case of MEX, the correlations between R_{TD} and

21699402, 2022, 5, Downloaded from https://agupubs.onlinelibrary.wiley.com/doi/10.1029/2021JA030146 by Cochrane France, Wiley Online Library on [23/11/2022]. See the Terms and Conditions (https://onlinelibrary.wiley.com/terms-and-conditions) on Wiley Online Library for rules of use; OA articles are governed by the applicable Creative Commons License

Table 1
Partial Correlation Analysis for the Angular Distance to and Location of the Strongest Crustal Source Region

Statistical parameters	MAVEN	MEX
Direct correlation coefficient R_{TD} versus angular distance (p-value)	−0.24 (n[a])	−0.12 (n)
Controled correlation coefficient R_{TD} versus angular distance (p-value)	−0.12 (n)	−0.11 (n)
Significance ratio t/t_{H_0} for angular distance	3.47	6.10
Relative influence $\frac{b^*_{EUV}}{b^*_{ang.dist.}}$	−3.73	−2.90
Direct correlation coefficient R_{TD} versus $\cos(\phi_{mso})$ (p-value)[b]	0.19 (n)	0.12 (n)
Controled correlation coefficient R_{TD} versus $\cos(\phi_{mso})$ (p-value)	0.09 (n)	0.11 (n)
Significance ratio t/t_{H_0} for $\cos(\phi_{mso})$	2.71	6.19
Relative influence $\frac{b^*_{EUV}}{b^*_{\cos(\phi_{mso})}}$	5.22	2.85

[a]"n" refers to negligible p-values ($<10^{-5}$). [b]ϕ_{mso} refers to the MSO longitude of the strongest crustal source region center.

both the angular distance and the longitude of the strongest crustal source region were only slightly reduced after controlling for EUV, while for MAVEN they were reduced by a factor 2 after controlling for EUV and Mms, thus reaching the MEX correlation levels (or close to for the longitude of the strongest crustal source region). This confirms the significant biases for the MAVEN dataset due to the EUV inhomogeneous distribution with respect to angular distance and longitude of the strongest crustal source region center, as well as the absence of bias for MEX. In both cases, the *t*-test statistics t is well above the t_{H_0} value that corresponds to the null hypothesis for a risk of 5%, corresponding to negligible or small p-values. Note that the significance levels of independent tests cannot be compared to each other to discuss the relative importance of variables, each test shall be considered individually.

The multiple linear regression used provides a rough estimate of the relative importance of the drivers included in the regression, by comparing the beta-weights (i.e., magnitudes of the coefficients). These are the slopes associated with each parameter of influence in the regression model, normalized by the ratio of the standard deviations of the BS terminator distance and of each parameter. The beta-weight of angular distance thus appears three to four times smaller than the EUV beta-weight for both MEX and MAVEN, suggesting a consistent relative influence that is smaller than EUV. Note that for MAVEN $\frac{b^*_{Mms}}{b^*_{ang.dist.}} \sim 4.1$ confirming that EUV and Mms are major drivers of the BS location. The beta-weight of ϕ_{mso} appears three to five times smaller than the beta-weight of EUV (with a smaller influence for MAVEN). The longitude of the strongest crustal source region center appears, based only on correlation coefficients, less than or as influent as the angular distance to the strongest crustal source region depending on the mission.

Note that a partial correlation analysis confirms that the crustal fields located in the nightside hemisphere have (little or) no influence on the BS location. Partial correlations between the shock location and the local crustal field pressure (after controlling for EUV and Mach number when available) for MEX and MAVEN, which are significant on the dayside despite being smaller than correlations with angular averaged crustal field pressures, become non-significant (with large p-values close to or larger than 5%) beyond the terminator. Using large-scale crustal field parameters (i.e., angular averaged pressure) instead of the local pressure also leads to reduced apparent influence beyond the terminator. However, the correlations still appear significant probably because the large scale parameters integrate to some extent dayside regions as well given the proximity of most of the nightside BS crossings with the terminator region.

The exact values of the statistical results shown above depend on the parameters included in the regression model (number of parameters, various methods to estimate the crustal magnetic field pressure instead of angular distance…), the chosen model (linear or power law), or on the conic parameters used to derive the R_{TD} altitudes, but the conclusions remain unchanged: the angular distance or crustal magnetic field pressure integrated over an angular range as well as the MSO longitude of the strongest crustal source region are significant drivers of the BS terminator distance - despite a bias in the MAVEN case due to the EUV distribution -, and EUV/Mms appear as the major drivers for the BS location.

21699402, 2022, 5, Downloaded from https://agupubs.onlinelibrary.wiley.com/doi/10.1029/2021JA030146 by Cochrane France, Wiley Online Library on [23/11/2022]. See the Terms and Conditions (https://onlinelibrary.wiley.com/terms-and-conditions) on Wiley Online Library for rules of use; OA articles are governed by the applicable Creative Commons License

We have in particular checked the robustness of the results by using different datasets (e.g., only the Gruesbeck et al. (2018) list or only the XF17 list) and various conic fit parameters (i.e., the parameters by Edberg et al. [2008]; Hall, Lester, S´anchez-Cano, et al. [2016], XF17 for either MAVEN or MEX): except for slightly different absolute altitudes, all results discussed above are unchanged.

The results show that empirical models representing the BS location should include the crustal fields whose influence is thus significant despite being of smaller importance compared to EUV or Mach number. A detailed analysis of the best functional form of the shock location combining all the BS location drivers is beyond the scope of this paper, but one can provide a simple empirical proxy that reflects the apparent influence of crustal fields with respect to EUV and Mach number based on our study. If one assumes a power law relation for the main drivers (EUV and Mach number for MAVEN) and for crustal fields, one can derive the power index values of each driver. For example, considering a simple relation such as $R_{TD} = a * K^{1/6} + b$ with a/b free constants and K a composite parameter defined by $K = EUV / \left(Mms * Ang_{dist}^{1/3} \right)$ (without the Mms parameter for MEX due to the absence of magnetic field) leads to correlation coefficients of 0.65/0.41 (n) for the MAVEN/MEX datasets, which are very strong correlation coefficients given a large amount of data. The 1/3 ratio is approximate but gives an order of magnitude of the relative influence of the EUV/Mach/crustal field drivers as given by a classic multivariate regression, or by partial correlation analysis (see e.g., Table 1) that provide slope ratios for specific drivers (with a slope ratio $\frac{b^*_{EUV}}{b^*_{Mms}}$ close to 1, and $\frac{b^*_{EUV\,or\,Mms}}{b^*_{ang.dist.}}$ around 3). Note that using power law or linear forms, or angular averaged crustal field pressure instead of angular distance to the strongest crustal field region, does not change these qualitative results.

This type of composite parameter is representative of the overall behavior of the shock location, but other drivers not studied in this paper shall be studied as well, such as the solar wind dynamic pressure, as well as the IMF intensity and orientation parameters. Moreover, investigating the relative influences in a complex system where numerous possible drivers can influence the BS location and can be cross correlated shall be performed with the use of specific techniques, as investigated in a forthcoming paper.

4. Discussion

Beyond the analysis of the global influence of crustal fields on the BS location, one can also investigate the seasonal variability of this influence. Figure 6 shows the compared seasonal variation of several parameters based on the Mars Express dataset that covered 6 martian years. We chose to focus on the Mars Express dataset which is more reliable than our MAVEN dataset which covers less than one martian year. The figure shows first how the influence of the strongest crustal field region on the MEX BS location varies with the solar longitude. The specific influence of the strongest crustal field region shown in the figure is defined as follows: we consider the crossings in the southern hemisphere latitude band of ±20° around the latitude of the strongest crustal field region center assumed at −45°, which was used in Section 3.1 to reveal a longitude modulation of the BS location; we then calculate the difference $R_{TD_{close_{mean}}} - R_{TD_{away_{mean}}}$ between the mean R_{TD} altitudes of the BS crossings close (120–240° East longitude range, see Figure 3d) versus away (0–120 and 240–360° East longitude) from the main source center located at ∼180° East longitude.

Figure 6 shows first that this R_{TD} difference is always positive, which is coherent with the strongest crustal field region pushing the BS further, with up to 400 km altitude difference. The figure also shows that the R_{TD} difference is maximum from about Ls ∼ 150° to Ls ∼ 250°, that is, from slightly before equinox until perihelion. The R_{TD} difference then shows a minimum around perihelion, at a period where the northern hemisphere is the most illuminated. Most of the crustal field sources are located in the southern hemisphere which is the most illuminated at the periods where the R_{TD} difference is maximum, which suggests a coupling with the ionosphere. The absolute R_{TD} altitude of the BS is expected to vary with the solar longitude due to the direct influence of ionization of the atmosphere, thus increasing the size of the obstacle through, for example, pickup ions and currents. However, one does not expect a priori a seasonal variability inside a given southern hemisphere latitude band between regions close and away from the main crustal field source region, unless a coupling exists between the ionosphere and the influence of the crustal field on the BS.

The figure also provides the seasonal variability of the Total Electron Content given by the MEX MARSIS instrument, showing in a similar manner the TEC difference $\left(TEC_{close_{mean}} - TEC_{away_{mean}} \right)$ between regions close

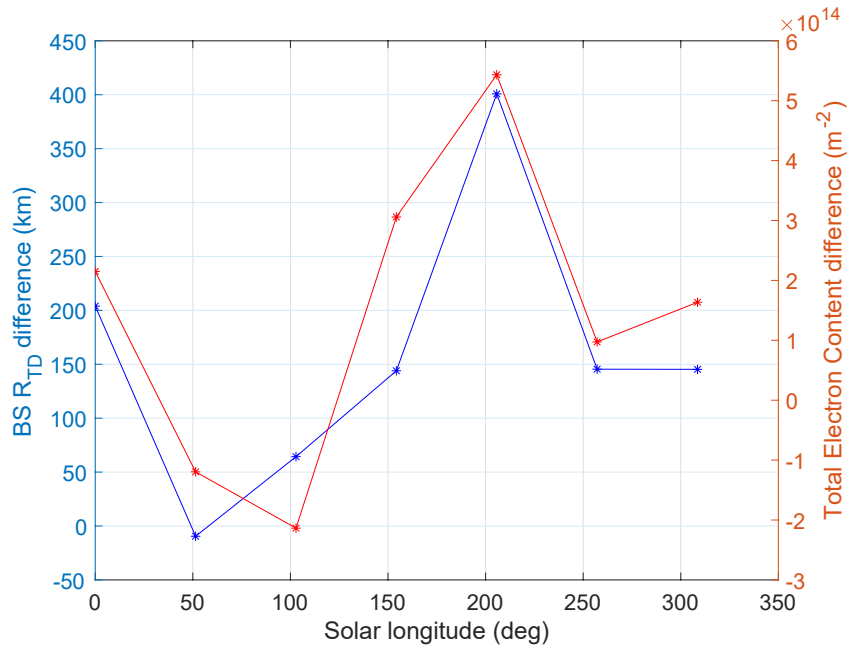


Figure 6. Compared seasonal variation of both the Total Electronic Content (TEC) of Mars ionosphere given by Mars Express (MEX) MARSIS data, and of the MEX bow shock R_{TD} extrapolated terminator altitudes. For both parameters at each season, we show the difference between the value close versus away the strongest crustal field source region (when only focusing on the southern hemisphere ±20° latitude band considered in Figure 1; see text for more details). The solar longitude (Ls) of Mars is the Mars-Sun angle measured from the Northern Hemisphere spring equinox where Ls = 0° (Ls = 90° corresponds to northern summer solstice, Ls = 180° to northern autumn equinox).

versus away from the strongest crustal field region in the southern latitude band ±20° around the center latitude −45°. The dataset. already analyzed in detail by Sánchez-Cano et al. (2021), is made of all TEC observations by MARSIS from Martian year 27 until Martian year 32.

One thus observes a strong correlation between the seasonal variability of the BS R_{TD} difference and the seasonal variability of the ionospheric TEC difference. Both profiles exhibit similar trends, with minima and maxima at the same seasons, in accordance with results by Sánchez-Cano et al. (2018). This strong correlation thus suggests that the seasonal variability of the influence of the strongest crustal field region on the BS is associated with the seasonal variability of the ionosphere. This confirms the presence of significant coupling processes between crustal fields and the ionosphere, and consequently with the BS location. The TEC is known to be a good tracer for not only the ionospheric variability, due to solar irradiance which is the major ionization source of the sunlit ionosphere, but also for the thermosphere-ionosphere coupling and possibly for the lower-upper atmosphere coupling. Several studies showed evidence of a coupling between the ionosphere and the crustal fields, resulting in increased ionospheric electron density - by 20%–50% - and reduced temperature in these regions (Flynn et al., 2017; González-Galindo et al., 2021). The density increase observed above crustal field regions was attributed to stable mechanisms instead of transient phenomena such as solar flares or enhanced particle precipitation. Ions newly formed by photoionization could be inhibited from diffusing out of the regions with strong crustal fields, resulting in higher densities (Duru et al., 2019) despite the stable ionization efficiencies in these regions (Lillis et al., 2021). Electrons trapped on closed field lines are indeed protected against loss mechanisms induced by the magnetosheath plasma and solar wind interaction, which leads to larger lifetimes and densities. The crustal fields thus impact the ionosphere characteristics, which then increases the local ionospheric pressure, and may push further the bow shock due to pressure enhancement and the inflation of the apparent obstacle to the solar wind via magnetosonic waves. For instance, the ionopause is known to be affected by the presence of crustal fields, with fewer ionopause detections over crustal fields since the increased local pressure (thermal + magnetic) makes it difficult for the SW dynamic pressure to penetrate, compress the ionosphere and form the ionopause (Sánchez-Cano et al., 2020).

21699402, 2022, 5, Downloaded from https://agupubs.onlinelibrary.wiley.com/doi/10.1029/2021JA030146 by Cochrane France, Wiley Online Library on [23/11/2022]. See the Terms and Conditions (https://onlinelibrary.wiley.com/terms-and-conditions) on Wiley Online Library for rules of use; OA articles are governed by the applicable Creative Commons License

21699402, 2022, 5, Downloaded from https://agupubs.onlinelibrary.wiley.com/doi/10.1029/2021JA030146 by Cochrane France, Wiley Online Library on [23/11/2022]. See the Terms and Conditions (https://onlinelibrary.wiley.com/terms-and-conditions) on Wiley Online Library for rules of use; OA articles are governed by the applicable Creative Commons License

The results above show that the coupling between crustal fields and the ionosphere plays a significant role in the influence of crustal fields on the BS location described in the previous sections. However, it remains difficult to conclude whether this coupling is the dominant process that takes place regarding the influence of crustal fields on the BS location, in addition to other processes such as the magnetic pressure enhancement due to crustal fields and the induced draping topology modification. This coupling has probably also had a significant influence on the other plasma boundaries such as the Induced Magnetospheric Boundary or the PhotoElectron Boundary which tightly depend on internal drivers. Further work will be performed to better characterize the complex coupling mechanisms that link the crustal fields to the TEC and ionosphere (and thus to the thermosphere) and to the induced magnetosphere up to the BS.

5. Conclusions

The recent studies of the Martian environment, thanks in particular to the MEX and MAVEN missions, underline the strong and complex influence of the crustal magnetic fields on the Martian environment and its interaction with the solar wind. Among them is the influence on the dynamic plasma boundaries that shape this interaction and on the bow shock (BS) in particular. Compared to other drivers of the BS location (e.g., SW dynamic pressure, extreme ultraviolet fluxes…), the crustal magnetic fields are poorly understood, with in the literature essentially differences observed between the southern and northern hemispheres attributed to the crustal fields, and an influence that ranges from little or no impact to strong influence depending on the authors and on the methods used. We analyzed in this paper in detail the influence of the crustal fields on the BS location, based on a one-dimensional approach using the extrapolated terminator distance of the shock crossings. This led to the following results:

1. Our study provides the first multi-mission detailed analysis of the poorly understood influence of the crustal fields on the Martian BS location, by studying datasets from two different spacecraft (MAVEN and MEX, including >15, 000 shock crossings) and using several methods that provide a coherent picture instead of a single point of views eventually contradictory as in previous works.
2. The crustal field sources on the Martian surface induce an influence on the BS location that is maximum when considering crustal field intensities or pressures (or even power law values of it) averaged an angular range of 70−80°, slightly less than a hemispheric asymmetry.
3. A number of crustal field source regions can play a role, from few nT intensity at a reference altitude of 400 km.
4. However, the strongest crustal field region in the southern hemisphere appears as the dominant driver.
5. We introduce the angular distance to the strongest crustal field region, which better reveals the influence of this region that is shown to extend between at least 40–60° angular distance (which is consistent with the size of this region) and a full hemisphere.
6. This influence may also be seen through the modulation of the BS location by a longitude modulation when focusing around southern latitudes (which reveals a stronger modulation than if all latitudes are included as in previous studies).
7. The crustal field influence is all the more reduced than the strongest crustal source region is located far from the noon direction, with a strong sinusoidal modulation by the local time of the strongest source region. This modulation is probably due to an increased travel time and attenuation for the magnetosonic wave until the solar wind upstream of the planet, combined with an expected larger Alfven velocity in the dayside draping region where the magnetic field increases.
8. Our analysis suggests that the crustal fields have no (eventually little) influence beyond the terminator region.
9. The influence of the strongest crustal field region appears more clearly when the IMF is stable during the preceding hours: the IMF usually rotates at short timescales, while the influence of the crustal fields is essentially a geographical influence in the planetary frame with a much larger timescale, which may partially mask its influence on the distant BS due to the rotation of the solar wind interaction.
10. We introduce a technique, that is, partial correlations (Baba et al., 2004), that allows for quantifying the influence of second-order importance drivers which may be hidden by the influence of correlated major drivers; this approach appears necessary to provide a coherent picture when considering several mission

datasets (MAVEN and MEX) where cross correlations exist (in particular for MAVEN), and it confirms the significant influence of the crustal fields on the Martian BS location.

11. We show the existence of a bias in the MAVEN data (but not in the MEX data) that leads to an incorrect estimation of the crustal field influence when authors focus only on north versus south hemispheric asymmetries during the same period of our dataset (2014-2017), since this asymmetry depends significantly on EUV conditions.
12. The partial correlation approach confirms that EUV and magnetosonic Mach number are major drivers of the BS location, while crustal fields are a significant but a second order driver of this boundary, with an induced variability of the order of several hundreds of km.
13. We provide a composite simple parameter that is representative of the overall behavior of the shock location with respect to EUV, magnetosonic Mach number and crustal fields, in a coherent manner for both MAVEN and MEX datasets.
14. We show the existence of seasonal variability of the influence of the strongest crustal field region on the BS.
15. Moreover, the seasonal variability of the crustal field influence is strongly correlated to the Total Electronic Content that is a tracer for the ionosphere dynamics and for its coupling with the thermosphere; our results reveal the existence of a large scale coupling between the crustal fields, the ionosphere and the BS (and probably with other plasma boundaries), presumably due to a density increase following the trapping of plasma on the closed field lines thus protected against loss mechanisms induced by the solar wind interaction.

Our study thus confirms the significant influence of crustal fields on the BS location based on a multi-mission analysis, describes in detail how this influence takes place (planetary longitude modulation, local time of and angular distance to the strongest crustal field region, crustal field pressure minimum threshold), and quantifies it spatial extent as well as its impact in terms of altitude of the BS. It also sheds a new light on the complexity of the influence of crustal fields on the martian environment, with an impact on the BS that is shown to be tightly coupled to both the ionosphere below (and possibly to the thermosphere through the TEC correlation observed) and to the IMF above that can modulate this influence through its rotation. This shows again how the martian environment is a complex fully connected system, where crustal fields make Mars a unique case.

In the future, we also plan to investigate the use of artificial intelligence techniques to provide automatic catalogs of plasma boundaries and eventually identify complex non-linear relationships between the boundaries' location and external/internal drivers. These techniques are mature and proved efficient in space physics to detect plasma phenomena (see e.g., Karimabadi et al., 2009; Nguyen et al., 2019) or to identify parameters of influence (see e.g., Al-Ghraibah et al., 2015; Benvenuto et al., 2018; Lenouvel et al., 2021).

Appendix A: Partial Correlation Approach

The partial correlation approach (Baba et al., 2004) investigates multiple regressions, calculating the correlation coefficients - and estimate their significance - between for example, two variables y and x_0, after controlling for the influence of other variables x_i. The correlations are assumed linear ($y = a + \sum_i x_i \cdot b_i$ with b_i constant individual slopes and a constant), but can correspond to power law relations of the type $y = a \prod_i x_i^{b_i}$ since the logarithm of the expression linearizes the expression.

For example, if one considers only three variables that are possibly correlated (x, y, z), the partial correlation between x and y, after controlling for z, is calculated as follows: first the linear regression between x and z is performed, and the residuals are given by the difference between the x values and the regression. Subtracting the regression line removes the influence of z on x. Residuals are then calculated for y with same procedure to remove the influence of z on y. The partial correlation coefficient between x and y, after controlling for the third variable z, is simply determined by the Pearson correlation coefficients between the two residuals. This technique can be generalized to a larger number of variables controlled.

The Pearson correlation coefficient between variables x_0 and y controlling for variables x_i ($i > 0$) are calculated recursively. The i + 1 order partial correlation coefficient is given by:

$$r_{x_0 y.x_1 \ldots x_i x_{i+1}} = \frac{r_{x_0 y.x_1 x_2 \ldots x_i} - r_{x_0 x_{i+1}.x_1 x_2 \ldots x_i} \cdot r_{y x_{i+1}.x_1 x_2 \ldots x_i}}{\sqrt{1 - r^2_{x_0 x_{i+1}.x_1 x_2 \ldots x_i}} \cdot \sqrt{1 - r^2_{y x_{i+1}.x_1 x_2 \ldots x_i}}} \quad \text{(A1)}$$

21699402, 2022, 5, Downloaded from https://agupubs.onlinelibrary.wiley.com/doi/10.1029/2021JA030146 by Cochrane France, Wiley Online Library on [23/11/2022]. See the Terms and Conditions (https://onlinelibrary.wiley.com/terms-and-conditions) on Wiley Online Library for rules of use; OA articles are governed by the applicable Creative Commons License

21699402, 2022, 5, Downloaded from https://agupubs.onlinelibrary.wiley.com/doi/10.1029/2021JA030146 by Cochrane France, Wiley Online Library on [23/11/2022]. See the Terms and Conditions (https://onlinelibrary.wiley.com/terms-and-conditions) on Wiley Online Library for rules of use; OA articles are governed by the applicable Creative Commons License

In order to evaluate the significance of the partial correlation factors with respect to the null hypothesis H0 (i.e., null correlation), the test statistics $t = \frac{r}{\sqrt{\frac{1-r^2}{n-3}}}$ is calculated. For a risk α (e.g., 5% in our case), the null hypothesis is rejected if $|t| > t_{H_0}$ where $t_{H_0} = t_{1-\alpha/2}(n-3)$ is the quantile of order $1 - \alpha/2$ of the Student law for $(n - 3)$ degrees of freedom. Similar to classic correlation coefficients, two-sided p-values can be determined to provide a probability that the null hypothesis is true: that is, the partial correlation is not significantly different from 0 as soon as the p-value is larger than the risk defined (5%).

Moreover, the quality evaluation of regression models, usually given by the determination coefficient R^2, monotonically increases with the number of variables included in the model. One thus needs to calculate the adjusted determination coefficient R'^2 to compare regression models including more or less variables, with:

$$R'^2 = 1 - \frac{n-1}{n-p-1}\left(1 - R^2\right) \tag{A2}$$

with n number of observations and p number of variables in the regression model, and $R^2 = 1 - \text{SSE}/\text{SST}$ with SSE the sum of squared error $\left(SSE = \sum_i \left(y_{i_{model}} - y_{mean}\right)^2\right)$ and SST the sum of squared total $\left(SST = \sum_i (y_i - y_{mean})^2\right)$.

Finally, the individual slopes b_i of variables x_i can be transformed into standardized slopes called beta-weights $\left(b_i^*\right)$ enabling to compare the relative influence of the variables (to avoid e.g., comparing different units or ranges): $b_i^* = b_i \frac{s_i}{s_y}$ with s_i and s_y the standard deviations of variables x_i and y.

Data Availability Statement

The MGS, MEX and MAVEN datasets of shock crossings are available in the https://doi.org/10.5281/zenodo.6240624 repository. All MGS, MEX and MAVEN instruments calibrated data are available on the AMDA web interface (http://amda.cdpp.eu, in the directory /Parameters/Resources/AMDA Database) as well as on the NASA Planetary Data System (https://pds-atmospheres.nmsu.edu/data_and_services/atmospheres_data/MAVEN/maven_main.html and https://pds-geosciences.wustl.edu/missions/mgs/index.htm) for MAVEN and MGS, and in the Planetary Science Archive (https://www.cosmos.esa.int/web/psa/mars-express) for MEX, with in particular the MARSIS data available at https://archives.esac.esa.int/psa/ftp/MARS-EXPRESS/MARSIS/.

Acknowledgments
This work was supported by the French space agency CNES. The authors acknowledge the support of the MAVEN and Mars Express instrument and science teams, as well as are the CDPP/AMDA team and E. Penou. B.S.-C acknowledges support through UK-STFC Ernest Rutherford Fellowship ST/V004115/1 and UK-STFC consolidated grant ST/S000429/1 and ST/W00089X/1. X.F acknowledges support through NASA grant 80NSSC19K0562.

References

Acuña, M. H., Connerney, J. E. P., Wasilewski, P., Lin, R. P., Anderson, K. A., Carlson, C. W., et al. (1992). Mars observer magnetic fields investigation. *Journal of Geophysical Research*, *97*(E5), 7799–7814. https://doi.org/10.1029/92JE00344

Acuña, M. H., Connerney, J. E. P., Wasilewski, P., Lin, R. P., Mitchell, D., Anderson, K. A., et al. (2001). Magnetic field of Mars: Summary of results from the aerobraking and mapping orbits. *Journal of Geophysical Research*, *106*(E10), 23403–23417. https://doi.org/10.1029/2000JE001404

Alexander, C. J., Luhmann, J. G., & Russell, C. T. (1986). Interplanetary field control of the location of the venus bow shock: Evidence for comet-like ion pickup. *Geophysical Research Letters*, *13*(9), 917–920. https://doi.org/10.1029/GL013i009p00917

Al-Ghraibah, A., Boucheron, L. E., & McAteer, R. T. J. (2015). An automated classification approach to ranking photospheric proxies of magnetic energy build-up. *Astronomy and Astrophysics*, *579*, A64. https://doi.org/10.1051/0004-6361/201525978

Anderson, R. B., & Bell, J. F. (2013). Correlating multispectral imaging and compositional data from the Mars exploration rovers and implications for Mars Science Laboratory. *Icarus*, *223*(1), 157–180. https://doi.org/10.1016/j.icarus.2012.11.029

Baba, K., Shibata, R., & Sibuya, M. (2004). Partial correlation and conditional correlation as measures of conditional independence. *Australian & New Zealand Journal of Statistics*, *46*(4), 657–664. https://doi.org/10.1111/j.1467-842X.2004.00360.x

Barabash, S., Lundin, R., Andersson, H., Brinkfeldt, K., Grigoriev, A., Gunell, H., et al. (2006). The analyzer of space plasmas and Energetic Atoms (ASPERA-3) for the Mars express mission. *Space Science Reviews*, *126*(1), 113–164. https://doi.org/10.1007/s11214-006-9124-8

Benvenuto, F., Piana, M., Campi, C., & Massone, A. M. (2018). A hybrid supervised/unsupervised machine learning approach to solar flare prediction. *The Astrophysical Journal*, *853*(1), 90. https://doi.org/10.3847/1538-4357/aaa23c

Bertaux, J.-L., Leblanc, F., Witasse, O., Quemerais, E., Lilensten, J., Stern, S. A., et al. (2005). Discovery of an aurora on Mars. *Nature*, *435*(7043), 790–794. https://doi.org/10.1038/nature03603

Brain, D. A., Lillis, R. J., Mitchell, D. L., Halekas, J. S., & Lin, R. P. (2007). Electron pitch angle distributions as indicators of magnetic field topology near Mars. *Journal of Geophysical Research*, *112*, A09201. https://doi.org/10.1029/2007JA012435

Cartacci, M., Amata, E., Cicchetti, A., Noschese, R., Giuppi, S., Langlais, B., et al. (2013). Mars ionosphere total electron content analysis from marsis subsurface data. *Icarus*, *223*(1), 423–437. https://doi.org/10.1016/j.icarus.2012.12.011

Cartacci, M., Sánchez-Cano, B., Orosei, R., Noschese, R., Cicchetti, A., Witasse, O., et al. (2018). Improved estimation of Mars ionosphere total electron content. *Icarus*, *299*, 396–410. https://doi.org/10.1016/j.icarus.2017.07.033

Chamberlin, P. C., Woods, T. N., & Eparvier, F. G. (2007). Flare irradiance spectral model (FISM): Daily component algorithms and results. *Space Weather*, *5*, S07005. https://doi.org/10.1029/2007SW000316

Connerney, J. E. P., Espley, J., Lawton, P., Murphy, S., Odom, J., Oliversen, R., & Sheppard, D. (2015). The MAVEN magnetic field investigation. *Space Science Reviews*, *195*, 257–291. https://doi.org/10.1007/s11214-015-0169-4

Crider, D. H. (2004). The influence of crustal magnetism on the solar wind interaction with Mars: Recent observations. *Advances in Space Research*, *33*(2), 152–160. https://doi.org/10.1016/j.asr.2003.04.013

Dai, Y. S., Wilkes, B. J., Bergeron, J., Kuraszkiewicz, J., Omont, A., Atanas, A., & Teplitz, H. I. (2018). Is there a relationship between AGN and star formation in IR-bright AGNs? *Monthly Notices of the Royal Astronomical Society*, *478*(3), 4238–4254. https://doi.org/10.1093/mnras/sty1341

DiBraccio, G. A., Luhmann, J. G., Curry, S. M., Espley, J. R., Xu, S., Mitchell, D. L., et al. (2018). The twisted configuration of the martian magnetotail: MAVEN observations. *Geophysical Research Letters*, *45*(10), 4559–4568. https://doi.org/10.1029/2018GL077251

Duru, F., Brain, B., Gurnett, D. A., Halekas, J., Morgan, D. D., & Wilkinson, C. J. (2019). Electron density profiles in the upper ionosphere of Mars from 11 years of marsis data: Variability due to seasons, solar cycle, and crustal magnetic fields. *Journal of Geophysical Research: Space Physics*, *124*(4), 3057–3066. https://doi.org/10.1029/2018JA026327

Edberg, N. J. T., Brain, D. A., Lester, M., Cowley, S. W. H., Modolo, R., Fränz, M., & Barabash, S. (2009). Plasma boundary variability at Mars as observed by Mars global surveyor and Mars express. *Annales Geophysicae*, *27*(9), 3537–3550. https://doi.org/10.5194/angeo-27-3537-2009

Edberg, N. J. T., Lester, M., Cowley, S. W. H., Brain, D. A., Fränz, M., & Barabash, S. (2010). Magnetosonic mach number effect of the position of the bow shock at Mars in comparison to venus. *Journal of Geophysical Research*, *115*(A7), A07203. https://doi.org/10.1029/2009JA014998

Edberg, N. J. T., Lester, M., Cowley, S. W. H., & Eriksson, A. I. (2008). Statistical analysis of the location of the martian magnetic pileup boundary and bow shock and the influence of crustal magnetic fields. *Journal of Geophysical Research*, *113*(A8), A08206. https://doi.org/10.1029/2008JA013096

Fang, X., Liemohn, M. W., Nagy, A. F., Luhmann, J. G., & Ma, Y. (2010). Escape probability of Martian atmospheric ions: Controlling effects of the electromagnetic fields. *Journal of Geophysical Research*, *115*(A4), A04308. https://doi.org/10.1029/2009JA014929

Fang, X., Ma, Y., Brain, D., Dong, Y., & Lillis, R. (2015). Control of Mars global atmospheric loss by the continuous rotation of the crustal magnetic field: A time-dependent mhd study. *Journal of Geophysical Research: Space Physics*, *120*(12), 10926–10944. https://doi.org/10.1002/2015JA021605

Fang, X., Ma, Y., Masunaga, K., Dong, Y., Brain, D., Halekas, J., et al. (2017). The Mars crustal magnetic field control of plasma boundary locations and atmospheric loss: Mhd prediction and comparison with maven. *Journal of Geophysical Research: Space Physics*, *122*(4), 4117–4137. https://doi.org/10.1002/2016JA023509

Flynn, C. L., Vogt, M. F., Withers, P., Andersson, L., England, S., & Liu, G. (2017). Maven observations of the effects of crustal magnetic fields on electron density and temperature in the martian dayside ionosphere. *Geophysical Research Letters*, *44*(21), 10812–10821. https://doi.org/10.1002/2017GL075367

Garnier, P., Steckiewicz, M., Mazelle, C., Xu, S., Mitchell, D., Holmberg, M. K. G., et al. (2017). The martian photoelectron boundary as seen by maven. *Journal of Geophysical Research: Space Physics*, *122*(10), 10472–10510. https://doi.org/10.1002/2017JA024497

González-Galindo, F., Eusebio, D., Němec, F., Peter, K., Kopf, A., Tellmann, S., & Paetzold, M. (2021). Seasonal and geographical variability of the martian ionosphere from Mars express observations. *Journal of Geophysical Research: Planets*, *126*(2), e2020JE006661. https://doi.org/10.1029/2020JE006661

Gruesbeck, J. R., Espley, J. R., Connerney, J. E. P., DiBraccio, G. A., Soobiah, Y. I., Brain, D., et al. (2018). The three-dimensional bow shock of Mars as observed by maven. *Journal of Geophysical Research: Space Physics*, *123*(6), 4542–4555. https://doi.org/10.1029/2018JA025366

Halekas, J. S., Ruhunusiri, S., Harada, Y., Collinson, G., Mitchell, D. L., Mazelle, C., et al. (2017). Structure, dynamics, and seasonal variability of the Mars-solar wind interaction: MAVEN solar wind ion analyzer in-flight performance and science results. *Journal of Geophysical Research*, *122*, 547–578. https://doi.org/10.1002/2016JA023167

Halekas, J. S., Taylor, E. R., Dalton, G., Johnson, G., Curtis, D. W., McFadden, J. P., et al. (2015). The solar wind ion analyzer for maven. *Space Science Reviews*, *195*(1), 125–151. https://doi.org/10.1007/s11214-013-0029-z

Hall, B. E. S., Lester, M., Nichols, J. D., Sánchez-Cano, B., Andrews, D. J., Opgenoorth, H. J., & Fränz, M. (2016). A survey of superthermal electron flux depressions, or "electron holes," within the illuminated martian induced magnetosphere. *Journal of Geophysical Research: Space Physics*, *121*(5), 4835–4857. https://doi.org/10.1002/2015JA021866

Hall, B. E. S., Lester, M., Sánchez-Cano, B., Nichols, J. D., Andrews, D. J., Edberg, N. J. T., et al. (2016). Annual variations in the martian bow shock location as observed by the Mars express mission. *Journal of Geophysical Research: Space Physics*, *121*(11), 11474–11511. https://doi.org/10.1002/2016JA023316

Hall, B. E. S., Sánchez-Cano, B., Wild, J. A., Lester, M., & Holmstrom, M. (2019). The martian bow shock over solar cycle 23â24 as observed by the Mars express mission. *Journal of Geophysical Research: Space Physics*, *124*(6), 4761–4772. https://doi.org/10.1029/2018JA026404

Kang, W.-Y., Wang, J.-X., Cai, Z.-Y., Guo, H.-X., Zhu, F.-F., Cao, X.-W., et al. (2018). An intrinsic link between long-term UV/optical variations and x-ray loudness in quasars. *The Astrophysical Journal*, *868*(1), 58. https://doi.org/10.3847/1538-4357/aae6c4

Karimabadi, H., Sipes, T. B., Wang, Y., Lavraud, B., & Roberts, A. (2009). A new multivariate time series data analysis technique: Automated detection of flux transfer events using Cluster data. *Journal of Geophysical Research*, *114*, A06216. https://doi.org/10.1029/2009JA014202

Kim, H.-J., Lyons, L., Boudouridis, A., Pilipenko, V., Ridley, A. J., & Weygand, J. M. (2011). Statistical study of the effect of ulf fluctuations in the imf on the cross polar cap potential drop for northward imf. *Journal of Geophysical Research*, *116*(A10), A10311. https://doi.org/10.1029/2011JA016931

Le, G.-M., & Zhang, X.-F. (2017). Dependence of large SEP events with different energies on the associated flares and *CMEs. Research in Astronomy and Astrophysics*, *17*(12), 123. https://doi.org/10.1088/1674-4527/17/12/123

Lenouvel, Q., Génot, V., Garnier, P., Toledo-Redondo, S., Lavraud, B., Aunai, N., et al. (2021). Identification of electron diffusion regions with a machine learning approach on MMS data at the Earth's magnetopause. *Earth and Space Science*, *8*(5), e01530. https://doi.org/10.1029/2020EA001530

Li, S., Lu, H., Cui, J., Yu, Y., Mazelle, C., Li, Y., et al. (2020). Effects of a dipole-like crustal field on solar wind interaction with Mars. *Earth and Planetary Physics*, *4*, 23–29. https://doi.org/10.26464/epp2020005

Lillis, R. J., & Brain, D. A. (2013). Nightside electron precipitation at Mars: Geographic variability and dependence on solar wind conditions. *Journal of Geophysical Research*, *118*(6), 3546–3556. https://doi.org/10.1002/jgra.50171

Lillis, R. J., Xu, S., Mitchell, D., Thiemann, E., Eparvier, F., Benna, M., & Elrod, M. (2021). Ionization efficiency in the dayside ionosphere of Mars: Structure and variability. *Journal of Geophysical Research: Planets*, *126*(12), e2021JE006923. https://doi.org/10.1029/2021JE006923

Ma, Y. J., Fang, X., Nagy, A. F., Russell, C. T., & Toth, G. (2014). Martian ionospheric responses to dynamic pressure enhancements in the solar wind. *Journal of Geophysical Research: Space Physics*, *119*, 1272–1286. https://doi.org/10.1002/2013JA019402

Masunaga, K., Seki, K., Brain, D. A., Fang, X., Dong, Y., Jakosky, B. M., et al. (2017). Statistical analysis of the reflection of incident O+ pickup ions at Mars: MAVEN observations. *Journal of Geophysical Research: Space Physics*, *122*(4), 4089–4101. https://doi.org/10.1002/2016JA023516

21699402, 2022, 5, Downloaded from https://agupubs.onlinelibrary.wiley.com/doi/10.1029/2021JA030146 by Cochrane France, Wiley Online Library on [23/11/2022]. See the Terms and Conditions (https://onlinelibrary.wiley.com/terms-and-conditions) on Wiley Online Library for rules of use; OA articles are governed by the applicable Creative Commons License

Matsunaga, K., Seki, K., Brain, D. A., Hara, T., Masunaga, K., Mcfadden, J. P., et al. (2017). Statistical study of relations between the induced magnetosphere, ion composition, and pressure balance boundaries around Mars based on MAVEN observations. *Journal of Geophysical Research: Space Physics*, *122*(9), 9723–9737. https://doi.org/10.1002/2017JA024217

Mazelle, C., Winterhalter, D., Sauer, K., Trotignon, J. G., Acuña, M. H., Baumgärtel, K., et al. (2004). Bow shock and upstream phenomena at Mars. *Space Science Reviews*, *111*(1), 115–181. https://doi.org/10.1023/B:SPAC.0000032717.98679.d0

Mitchell, D. L., Lin, R. P., Mazelle, C., Rème, H., Cloutier, P. A., Connerney, J. E. P., et al. (2001). Probing Mars' crustal magnetic field and ionosphere with the MGS Electron Reflectometer. *Journal of Geophysical Research*, *106*, 23419–23427. https://doi.org/10.1029/2000JE001435

Mitchell, D. L., Mazelle, C., Sauvaud, J.-A., Thocaven, J.-J., Rouzaud, J., Fedorov, A., et al. (2016). The MAVEN solar wind electron analyzer. *Space Science Reviews*, *200*, 495–528. https://doi.org/10.1007/s11214-015-0232-1

Morschhauser, A., Lesur, V., & Grott, M. (2014). A spherical harmonic model of the lithospheric magnetic field of Mars. *Journal of Geophysical Research*, *119*, 1162–1188. https://doi.org/10.1002/2013JE004555

Nemec, F., Linzmayer, V., Nemecek, Z., & Safrankova, J. (2020). Martian bow shock and magnetic pileup boundary models based on an automated region identification. *Journal of Geophysical Research: Space Physics*, *125*, e2020JA028509. https://doi.org/10.1029/2020JA028509

Nguyen, G., Aunai, N., Fontaine, D., Le Pennec, E., Van den Bossche, J., Jeandet, A., et al. (2019). Automatic detection of interplanetary coronal mass ejections from in situ data: A deep learning approach. *The Astrophysical Journal*, *874*(2), 145. https://doi.org/10.3847/1538-4357/ab0d24

Ni, Q., Brandt, W. N., Yang, G., Leja, J., Chen, C.-T. J., Luo, B., et al. (2020). Revealing the relation between black hole growth and host-galaxy compactness among star-forming galaxies. *Monthly Notices of the Royal Astronomical Society*, *500*(4), 4989–5008. https://doi.org/10.1093/mnras/staa3514

Poppe, A. R., Brain, D. A., Dong, Y., Xu, S., & Jarvinen, R. (2021). Particle-in-cell modeling of martian magnetic Cusps and their role in enhancing nightside ionospheric ion escape. *Geophysical Research Letters*, *48*(1), e90763. https://doi.org/10.1029/2020GL090763

Romanelli, N., Modolo, R., Leblanc, F., Chaufray, J. Y., Hess, S., Brain, D., et al. (2018). Effects of the crustal magnetic fields and changes in the IMF orientation on the magnetosphere of Mars: MAVEN observations and LatHyS results. *Journal of Geophysical Research: Space Physics*, *123*(7), 5315–5333. https://doi.org/10.1029/2017JA025155

Sánchez-Cano, B., Lester, M., Cartacci, M., Orosei, R., Witasse, O., Blelly, P.-L., & Kofman, W. (2021). Ionosphere of Mars during the consecutive solar minima 23/24 and 24/25 as seen by marsis-Mars express. *Icarus*, 114616. https://doi.org/10.1016/j.icarus.2021.114616

Sánchez-Cano, B., Lester, M., Witasse, O., Blelly, P.-L., Indurain, M., Cartacci, M., et al. (2018). Spatial, seasonal, and solar cycle variations of the martian total electron content (tec): Is the tec a good tracer for atmospheric cycles? *Journal of Geophysical Research: Planets*, *123*(7), 1746–1759. https://doi.org/10.1029/2018JE005626

Sánchez-Cano, B., Morgan, D. D., Witasse, O., Radicella, S. M., Herraiz, M., Orosei, R., et al. (2015). Total electron content in the martian atmosphere: A critical assessment of the Mars express marsis data sets. *Journal of Geophysical Research: Space Physics*, *120*(3), 2166–2182. https://doi.org/10.1002/2014JA020630

Sánchez-Cano, B., Narvaez, C., Lester, M., Mendillo, M., Mayyasi, M., Holmstrom, M., et al. (2020). Mars' ionopause: A matter of pressures. *Journal of Geophysical Research: Space Physics*, *125*(9), e2020JA028145. https://doi.org/10.1029/2020JA028145

Schneider, N. M., Jain, S. K., Deighan, J., Nasr, C. R., Brain, D. A., Larson, D., et al. (2018). Global aurora on Mars during the September 2017 space weather event. *Geophysical Research Letters*, *45*(15), 7391–7398. https://doi.org/10.1029/2018gl077772

Simms, L. E., Engebretson, M. J., Rodger, C. J., Dimitrakoudis, S., Mann, I. R., & Chi, P. J. (2021). The combined influence of lower band chorus and ulf waves on radiation belt electron fluxes at individual l-shells. *Journal of Geophysical Research: Space Physics*, *126*(5), e2020JA028755. https://doi.org/10.1029/2020JA028755

Steckiewicz, M., Garnier, P., André, N., Mitchell, D. L., Andersson, L., Penou, E., et al. (2017). Comparative study of the martian suprathermal electron depletions based on Mars global surveyor, Mars express, and Mars atmosphere and Volatile EvolutioN mission observations. *Journal of Geophysical Research: Space Physics*, *122*, 857–873. https://doi.org/10.1002/2016JA023205

Trottet, G., Samwel, S., Klein, K. L., Dudok De Wit, T., & Miteva, R. (2015). Statistical evidence for contributions of flares and coronal mass ejections to major solar energetic particle events. *Solar Physics*, *290*(3), 819–839. https://doi.org/10.1007/s11207-014-0628-1

Vignes, D., Acuna, M. H., Connerney, J. E. P., Crider, D. H., Reme, H., & Mazelle, C. (2002). Factors controlling the location of the bow shock at Mars. *Geophysical Research Letters*, *29*(9), 421. https://doi.org/10.1029/2001GL014513

Wang, M., Lu, J. Y., Kabin, K., Yuan, H. Z., Ma, X., Liu, Z.-Q., et al. (2016). The influence of IMF clock angle on the cross section of the tail bow shock. *Journal of Geophysical Research: Space Physics*, *121*(11), 11077–11111. https://doi.org/10.1002/2016JA022830

Xu, S., Mitchell, D., Liemohn, M., Dong, C., Bougher, S., Fillingim, M., et al. (2016). Deep nightside photoelectron observations by MAVEN SWEA: Implications for Martian northern hemispheric magnetic topology and nightside ionosphere source. *Geophysical Research Letters*, *43*, 8876–8884. https://doi.org/10.1002/2016GL070527

Yesuf, H. M., & HoL, C. (2019). Dirt-cheap gas scaling relations: Using dust absorption, metallicity, and galaxy size to predict gas masses for large samples of galaxies. *The Astrophysical Journal*, *884*(2), 177. https://doi.org/10.3847/1538-4357/ab4202

21699402, 2022, 5, Downloaded from https://agupubs.onlinelibrary.wiley.com/doi/10.1029/2021JA030146 by Cochrane France, Wiley Online Library on [23/11/2022]. See the Terms and Conditions (https://onlinelibrary.wiley.com/terms-and-conditions) on Wiley Online Library for rules of use; OA articles are governed by the applicable Creative Commons License